

A greedy non-intrusive reduced order model for shallow water equations

Sourav Dutta^a, Matthew W. Farthing^a, Emma Perracchione^b, Gaurav Savant^a, Mario Putti^b

^a*U.S. Army Engineer Research and Development Center, Coastal and Hydraulics Laboratory (ERDC-CHL), Vicksburg, MS 39180, USA.*

^b*Department of Mathematics “Tullio Levi-Civita”, University of Padova, Padova, Italy*

Abstract

In this work, we develop Non-Intrusive Reduced Order Models (NIROMs) that combine Proper Orthogonal Decomposition (POD) with a Radial Basis Function (RBF) interpolation method to construct efficient reduced order models for time-dependent problems arising in large scale environmental flow applications. The performance of the POD-RBF NIROM is compared with a traditional nonlinear POD (NPOD) model by evaluating the accuracy, robustness, and speed for test problems representative of riverine flows. Different greedy algorithms are studied in order to determine a near-optimal distribution of interpolation points for the RBF approximation. A new power-scaled residual greedy (*psr-greedy*) algorithm is proposed that overcomes the drawbacks of the existing greedy approaches to enhance the accuracy and efficiency of the RBF approximation. The relative performance of these greedy algorithms is studied with numerical experiments using realistic 2D shallow water flow applications involving coastal and riverine dynamics.

Keywords: Shallow water equations, Non-intrusive reduced order model, Radial basis function interpolation, Proper orthogonal decomposition, Greedy algorithms

2010 MSC: 41A05, 65D05, 65M60

1. Introduction

The shallow water equations (SWE) are used to model a wide variety of free-surface problems found across science and engineering, ranging from dam breaks [1] and riverine hydrodynamics to hurricane storm surge [2] and atmospheric processes [3]. Despite the trend of hardware improvements and significant gains in the algorithmic efficiency of standard discretization procedures, *high-fidelity* numerical resolution of shallow water models can still be very computationally intensive, due to the large amount of degrees of freedom (DOFs) needed to solve the PDE [4, 5]. The resulting computational expense poses a barrier to the inclusion of fully resolved two-dimensional shallow water models in many-query and

Email addresses: Sourav.Dutta@erdc.dren.mil (Sourav Dutta),
Matthew.W.Farthing@erdc.dren.mil (Matthew W. Farthing),
emma.perracchione@math.unipd.it (Emma Perracchione)

real-time applications, particularly when the analysis involves optimal design, parameter estimation, risk assessment, and/or uncertainty quantification. *Reduced order models* (ROMs) offer a valuable alternative way to simulate such dynamical systems with considerably reduced computational cost in comparison to the high-fidelity model (HFM). The objective of these approaches is to replace the high-fidelity model by one with significantly reduced dimensions, thus trading in computational burden for a controlled loss of accuracy [6].

Reduced basis (RB) methods [4, 7, 8] constitute a family of widely popular ROM techniques which are usually implemented with an offline-online decomposition paradigm. The *offline* stage involves the construction of a solution-dependent basis spanned by a set of RB “modes”, which are extracted from a collection of high-fidelity solutions, also called *snapshots*. The RB “modes” can be thought of as a set of global basis functions that can approximate the dynamics of the high-fidelity model. The most well known method to extract the reduced basis is called *proper orthogonal decomposition* (POD) [9, 10], which is particularly effective when the coherent structures of the flow can be hierarchically ranked in terms of their energy content. In this method, a truncated Singular Value Decomposition (SVD) of the snapshot matrix produces a low rank global basis of the most significant empirical modes, that are optimal with respect to the L^2 norm [11]. The POD method has been successfully applied in various fields and is often referred to by different names. For instance, it is termed principal component analysis (PCA) method in statistics [12], and the Karhunen-Loeve decomposition in signal analysis and pattern recognition [13]. The POD technique has also been applied to ocean models [14], air pollution models [15], convective Boussinesq flows [16], and SWE models [17, 18, 19, 20, 21]. In the last decade, Koopman mode theory [22] has also provided a rigorous theoretical background for an efficient modal decomposition in problems describing oscillations and other nonlinear dynamics using a technique called dynamic mode decomposition (DMD) [23]. Several variants of the DMD algorithm have been successfully applied as a modal decomposition tool in nonlinear dynamics [24, 25, 26] and has also been adopted as an alternative for POD in the determining the most optimal global basis modes for nonlinear problems [17, 27, 28, 29].

In the *online* stage, a linear combination of the reduced order RB modes is used to approximate the truth solution (high-fidelity numerical solution) for a new configuration of flow parameters. The procedure adopted to compute the expansion coefficients leads to the classification of RB methods into two broad categories: *intrusive* and *non-intrusive*. In an intrusive RB method, the expansion coefficients are determined by the solution of a reduced order system of equations, which is typically obtained via a Galerkin or Petrov-Galerkin projection of the high-fidelity (full-order) system onto the RB space [21]. For linear systems, the POD/Galerkin projection is the most popular choice. However, in the presence of nonlinearities, an affine expansion of the nonlinear (or non-affine) differential operator must be recovered in order to make the evaluation of the projection-based reduced model independent of the number of DOFs of the high-fidelity solution. Several different techniques, collectively referred to as hyper-reduction methods [30], have been proposed to address this problem. Barrault *et al.* [31] proposed the empirical interpolation method (EIM) that constructs an approximation of the non-affine parametrized function. Chaturantabut and Sorensen [32] proposed a discrete empirical interpolation method (DEIM) in which, using a collocation-based strategy,

the reduced approximation is enforced to match the nonlinear function at a specific number of sampling points. The “gappy POD” method [33] similarly minimizes the least squares error on the set of sampled points to seek the most optimal reduced approximation. Several other methods have also been proposed, namely a coefficient-function approximation consisting of a linear combination of precomputed basis functions [34], and a combination of a quadratic expansion method and the DEIM called the residual DEIM method [35]. Moreover, in complex nonlinear problems some of the intrinsic structures present in the high-fidelity model may be lost during order reduction using the projection-based POD/Galerkin approaches. This can result in qualitatively wrong solutions or instability issues [36, 37, 38]. As a remedy, Petrov-Galerkin projection based approaches have been proposed [39, 40]. Alternatively, introducing a diffusion term into the reduced model [41], has also been shown to improve the stability of ROM results.

A valuable alternative family of methods to address the issues of instability and loss of efficiency in the presence of more general, non-affine differential operators is represented by *non-intrusive* reduced order models (NIROMs). The primary advantage of this class of methods is that complex modifications to the source code describing the physical model can be avoided, thus making it easier to develop reduced models when the source code is not available or easily modifiable, which can often be the case for legacy and commercial codes. In these methods, instead of a Galerkin-type projection, the expansion coefficients for the reduced solution are obtained via interpolation on the space of a reduced basis extracted from snapshot data. However, since the reduced bases generally belong to nonlinear, matrix manifolds, a variety of interpolation techniques have been proposed that are capable of enforcing the constraints characterizing those manifolds. Regression-based non-intrusive methods have been proposed that, among others, use artificial neural networks (ANNs), in particular multi-layer perceptrons [42] as well as Gaussian process regression (GPR) [43, 44] to perform the interpolation.

Radial Basis Function (RBF) interpolation is another effective tool for interpolation of multidimensional scattered data [45] and has been demonstrated to be flexible, convenient and accurate in various research areas [46, 47, 48]. Adopting RBF interpolation for extracting the coefficients of the reduced basis has been shown to be quite successful for nonlinear, time dependent PDEs [49], nonlinear, parametrized PDEs [50, 51, 52], and aerodynamic shape optimization [53], to name a few. However, in most of the current non-intrusive ROMs the dimensional size is $N_c = N_s \times \sum_{i=1}^d m_i$, where N_s is the number of snapshots collected, d denotes the number of system components and m_i is the number of truncated POD modes selected for the i^{th} component. This can sometimes lead to excessive computational costs due to the exponential increase in the size of the multidimensional basis used in the RBF interpolation process. To address this issue, Xiao *et al.* [49] presented a Smolyak sparse grid collocation approach to construct the interpolation functions, while an adaptive greedy sampling approach was proposed by Chen *et al.* [52] to select an optimal basis in the offline stage.

In this work, we present a greedy non-intrusive reduced order model for the SWE in *fast replay* applications. The high-fidelity numerical model adopted for the solution of the SWE is based on a continuous Galerkin (CG) finite element (FE) approximation [54]. To

prevent non-physical oscillations in the solution, a residual-based stabilization is used that is essentially an extension of the original Streamline Upwind Petrov Galerkin (SUPG) [55, 56] approach. The RBF-POD NIROM model differs from the model presented in [49], by using RBF interpolation to approximate the time derivative of the reduced coefficients, thus adding flexibility to represent more general time-dependent problems. In this approach, appropriate POD modes are obtained from the collected snapshots by an application of the truncated SVD. The RBF multidimensional interpolation method is then used to generate an interpolation function that advances the reduced solution in time. The novelty of this work lies in the choice of interpolating the temporal derivative of the POD modes and the greedy selection of snapshot information to generate the RBF interpolant itself. The goal is to provide improved flexibility and efficiency in approximating online temporal dynamics. Specifically, three different greedy algorithms are studied for the selection of an optimal subset of the collected snapshots as the centers for the radial kernel in order to improve the efficiency of the RBF NIROM. The *p-greedy* [57] algorithm is designed to optimize the selection of centers based on an iterative minimization of the error introduced by the kernel properties and measured by the power function. The *f-greedy* [58] algorithm directly minimizes the residual error in the RBF approximation for every mode of the reduced coefficients and a greedy strategy is proposed for an efficient implementation in a multidimensional interpolation setting. Finally, a novel power-scaled greedy or *psr-greedy* algorithm is introduced that minimizes the scaled residual error where the power function is adopted as the variable scaling factor. The greedily obtained set of centers is used to construct a multidimensional RBF interpolant for approximating the time derivative of the projected snapshots. In the online stage, this RBF interpolant is employed to compute reduced solutions for any new time configuration queried by the fast-replay application.

The paper is organized as follows. In Section 2, we present the general SWE in two dimensions for depth-averaged, free-surface flows and then summarize the SUPG-stabilized, CG high-fidelity numerical method. In Section 3, the traditional nonlinear POD (NPOD) global model reduction technique via SVD-basis collection and subsequent Galerkin projection is presented, and relevant details for its application to the discrete, stabilized high-fidelity SWE model are provided. Section 4.1 provides a preliminary introduction to the theory of kernel-based approximation, while in Section 4.2, the multidimensional POD-RBF NIROM is introduced, that uses the projected HFM snapshots to construct the RBF interpolant for online evaluations of the reduced model. In Section 4.3 three different adaptive greedy sampling strategies are proposed for an improved selection of near-optimal interpolation points to be used in constructing the RBF interpolant. Numerical tests have been performed for tidal flows with temporally varying boundary forcing, as well as riverine flows and the results are provided in Section 5, with a careful examination of both the accuracy and the relative efficiency. Section 6 provides a brief review of some of the salient features of the NIROM framework. Finally, in Section 7, the concluding remarks are presented.

2. High-fidelity formulation for the shallow water equations

2.1. Continuous formulation

For our high-fidelity model, we consider a standard depth-averaged SWE formulation written as [59]

$$\mathcal{R} \equiv \frac{\partial \mathbf{q}}{\partial t} + \frac{\partial \mathbf{p}_x}{\partial x} + \frac{\partial \mathbf{p}_y}{\partial y} + \mathbf{r} = 0, \quad (1)$$

with $\mathbf{q} = [q_1, q_2, q_3]^T$ the unknown conservation variable consisting of the flow depth, $q_1 = h$, and discharges in the x and y directions given by $q_2 = u_x h$ and $q_3 = u_y h$, respectively. Here u_x is the velocity in the x direction and u_y is the velocity in the y direction. In addition to the conservation variable \mathbf{q} , we will also make direct reference to the primitive state variable $\mathbf{u} = [u_1, u_2, u_3]^T = [h, u_x, u_y]^T$ in some cases below as well. The flux vectors in the lateral directions are

$$\mathbf{p}_x = \left\{ \begin{array}{c} u_x h \\ u_x^2 h + (1/2)gh^2 - h(\sigma_{xx}/\rho) \\ u_x u_y h - h(\sigma_{yx}/\rho) \end{array} \right\}, \quad (2)$$

$$\mathbf{p}_y = \left\{ \begin{array}{c} u_y h \\ u_x u_y h - h(\sigma_{xy}/\rho) \\ u_y^2 h + (1/2)gh^2 - h(\sigma_{yy}/\rho) \end{array} \right\}, \quad (3)$$

and

$$\mathbf{r} = \left\{ \begin{array}{c} 0 \\ gh \frac{\partial h_b}{\partial x} + gh \left[(n_{mn}^2 u_x \sqrt{u_x^2 + u_y^2}) / h^{4/3} \right] - f_c h u_y \\ gh \frac{\partial h_b}{\partial y} + gh \left[(n_{mn}^2 u_y \sqrt{u_x^2 + u_y^2}) / h^{4/3} \right] + f_c h u_x \end{array} \right\}, \quad (4)$$

where we have written eqs. (2)-(4) in terms of the primitive variables for convenience. Here, ρ is the fluid density, g is the gravitational acceleration, and h_b is the elevation of the bottom surface. f_c is the Coriolis coefficient, and a standard Manning's parameterization for bottom roughness is used in eq. (4) with coefficient n_{mn} . $\sigma_{xx,xy,yx,yy}$ are Reynolds stresses due to turbulence which are approximated using the Boussinesq approach for the gradient in the mean currents

$$\sigma_{xx} = 2\rho\nu_t \frac{\partial u_x}{\partial x}, \quad (5)$$

$$\sigma_{yy} = 2\rho\nu_t \frac{\partial u_y}{\partial y}, \text{ and} \quad (6)$$

$$\sigma_{xy} = \sigma_{yx} = 2\rho\nu_t \left(\frac{\partial u_x}{\partial y} + \frac{\partial u_y}{\partial x} \right), \quad (7)$$

where ν_t is the kinematic eddy viscosity [1].

2.2. Stabilized finite element scheme for the semi-discrete weak formulation

Given a spatial domain $\Omega \subset \mathbb{R}^2$, temporal domain $[0, T]$, and a suitable test space \mathbf{W} defined on Ω , the classical weak form for eq. (1) can be written as

$$\int_{\Omega} \frac{\partial \mathbf{q}}{\partial t} \mathbf{w} \, dx - \int_{\Omega} \left(\frac{\partial \mathbf{w}}{\partial x} \mathbf{p}_x + \frac{\partial \mathbf{w}}{\partial y} \mathbf{p}_y \right) \, dx + \int_{\partial\Omega} (\mathbf{p}_x n_x + \mathbf{p}_y n_y) \mathbf{w} \, ds + \int_{\Omega} \mathbf{r} \mathbf{w} \, dx = 0, \quad (8)$$

where \mathbf{w} is an arbitrary test function in \mathbf{W} and $\mathbf{n} = [n_x, n_y]^T$ is the outer unit normal for Ω . Note that we have integrated the divergence terms in eq. (1) by parts and assume that eq. (8) holds for $t \in [0, T]$. If we denote ξ_s as the s -th basis function from a standard piece-wise linear CG approximation space, then the discrete solution $q_{h,i}$ ($i = 1, 2, 3$), to the weak problem given by eq. (8) can be represented as $q_{h,i} = \sum_{s=1}^N \xi_s q_{i,s}$, where $\hat{\mathbf{q}}_i = [q_{i,1}, \dots, q_{i,N}]^T$, ($i = 1, 2, 3$), are the N dimensional coefficient vectors for each solution component. Similarly, the primitive variables can be represented in terms of ξ_s as $u_{h,i} = \sum_{s=1}^N \xi_s u_{i,s}$, with N -dimensional coefficient vectors $\hat{\mathbf{u}}_i = [u_{i,1}, \dots, u_{i,N}]^T$, ($i = 1, 2, 3$). Unfortunately, straightforward Galerkin approximations to eq. (8) fail to produce accurate solutions in a number of flow regimes [60]. In particular, advection-dominated conditions with shocks or near-shocks are particularly challenging. For this reason, we use residual-based stabilization from [61] which is an extension of the original SUPG method [56, 62]. Letting \mathbf{w}_h be an arbitrary test function in \mathbf{W}_h , we write

$$\begin{aligned} & \int_{\Omega} \frac{\partial \mathbf{q}_h}{\partial t} \mathbf{w}_h \, dx - \int_{\Omega} \left(\frac{\partial \mathbf{w}_h}{\partial x} \mathbf{p}_x + \frac{\partial \mathbf{w}_h}{\partial y} \mathbf{p}_y \right) \, dx + \int_{\partial\Omega} (\mathbf{p}_x n_x + \mathbf{p}_y n_y) \mathbf{w}_h \, ds \\ & + \int_{\Omega} \mathbf{r} \mathbf{w}_h \, dx + \sum_e \int_{\Omega_e} \mathcal{R}_h \left[(\mathbf{J}_x \boldsymbol{\tau}_x)^T \frac{\partial \mathbf{w}_h}{\partial x} + (\mathbf{J}_y \boldsymbol{\tau}_y)^T \frac{\partial \mathbf{w}_h}{\partial y} \right] \, dx = 0. \end{aligned} \quad (9)$$

Here, $\mathbf{J}_{x,y} = \mathbf{p}'_{x,y}$ are the advective flux Jacobians, $\{\Omega_e\}_1^{N_e}$ is the collection of elements in a simplicial triangulation of Ω , and \mathcal{R}_h is an approximation of the strong residual \mathcal{R} . The specific form of the intrinsic time scale parameters, $\boldsymbol{\tau}_{x,y}$, can be found in [54].

There are a range of boundary conditions that can be incorporated into eq. (9) in practice. For example, at riverine inflow boundaries we will consider normal flux conditions on the total discharge,

$$q_2 n_x + q_3 n_y = (u_x h) n_x + (u_y h) n_y = q_b. \quad (10)$$

At land boundaries, a no-flow condition $u_x n_x + u_y n_y = 0$ holds, while at sea boundaries, the free surface elevation $\eta = h + h_b = \eta_b$, is specified. Radiation boundary conditions may also be specified as well [54].

2.3. Time discretization

For the temporal discretization of eq. (9), we consider a second-order backward Euler (BDF-2) approximation in which the nonlinear terms from eq. (9) are extrapolated in time. The time derivatives in the continuity and momentum equations are expressed as

$$\left(\frac{\partial q}{\partial t}\right)_i^{n+1} = \alpha \left[\frac{(3/2q_i^{n+1} - 1/2q_i^n) - (3/2q_i^n - 1/2q_i^{n-1})}{\Delta t} \right] + (1 - \alpha) \left[\frac{q_i^{n+1} - q_i^n}{\Delta t} \right], \quad (11)$$

where $0 \leq \alpha \leq 1$ is a factor that determines the order of time stepping, Δt is the time step size and the superscript n indicates the n^{th} time step, so that the actual time is $t^n = n\Delta t$.

After introducing the time discretization (11) in eq. (9), we can recover a fully discrete nonlinear system in the primitive variables at time step t^{n+1} as

$$\mathbf{R}_u^{n+1}(\mathbf{u}_h^{n+1}) = 0, \quad (12)$$

where $\mathbf{u}_h = [\widehat{\mathbf{u}}_1^T, \widehat{\mathbf{u}}_2^T, \widehat{\mathbf{u}}_3^T]^T$. In terms of the conservative variables, the discrete nonlinear system can be written as $\mathbf{R}_q^{n+1}(\mathbf{q}_h^{n+1}) = 0$ where $\mathbf{q}_h = [\widehat{\mathbf{q}}_1^T, \widehat{\mathbf{q}}_2^T, \widehat{\mathbf{q}}_3^T]^T$.

3. Global basis reduced order model

One of the main advantages of a projection-based reduced model framework is the systematic splitting of the computational procedure into a resource intensive offline stage and an efficient online stage, either in a real-time or many-query context. The offline stage comprises simulations carried out with the high-fidelity numerical model introduced in Section 2. It is assumed that the temporal and spatial resolutions adopted are sufficient to extract all the relevant dynamics and key features of the flow. In the online stage, due to lack of computational resources and/or time constraints, a more efficient model (i.e. ROM) with possible relaxed accuracy is required and an efficient ROM that leverages the fine-scale information collected in the offline stage is introduced.

The non-intrusive ROM approach proposed in this work comprises of two additional steps in the offline computations. First, the high dimensional solution to the dynamical system is represented in a low-dimensional subspace that is constructed by choosing the most significant (in terms of energy) global empirical basis modes obtained by POD. Second, a multivariate RBF interpolant is adopted to capture the time evolution of the low-dimensional snapshots. The projection of the governing equations to the space of POD modes is avoided, which circumvents the need for any additional stabilization of the ROM to account for the nonlinearity in the governing equations.

3.1. Proper Orthogonal Decomposition

POD is arguably the most popular projection-based model reduction method and has been successfully applied to a host of large-scale dynamical systems [63]. We use a generic algebraic formulation of dynamical systems to present a brief overview of the procedure.

We first introduce a generic vector of $3N$ degrees of freedom, $\mathbf{v} = [\mathbf{v}_1^T, \mathbf{v}_2^T, \mathbf{v}_3^T]^T$, which can represent either the discrete conservation variables, $[\widehat{\mathbf{q}}_1^T, \widehat{\mathbf{q}}_2^T, \widehat{\mathbf{q}}_3^T]^T$ or the discrete primitive variables $[\widehat{\mathbf{u}}_1^T, \widehat{\mathbf{u}}_2^T, \widehat{\mathbf{u}}_3^T]^T$. Then let $\widetilde{\mathbf{S}}_i = [\mathbf{v}_i^1, \dots, \mathbf{v}_i^M]$ be an $N \times M$ matrix of solution snapshots, $M \leq N$, obtained from the high-fidelity offline computations from time $t = 0$ to $t = T$ for each of the three state variables, using potentially variable time steps. It is assumed that the set $\widetilde{\mathbf{S}}_i$ captures all the key features of the flow phenomena. Following the usual practice [64], a new “normalized” set of snapshots \mathbf{S}_i is generated by removing the time averaged value from each of the snapshots in $\widetilde{\mathbf{S}}_i$ such that $\mathbf{S}_i = (\mathbf{v}_i^1 - \bar{\mathbf{v}}_i, \dots, \mathbf{v}_i^M - \bar{\mathbf{v}}_i)$ where $\bar{\mathbf{v}}_i = \sum_{n=1}^M \mathbf{v}_i^n / M$. In some cases, the initial condition is used to offset the set of snapshots [41, 65], while the solution itself may also be used to build the basis representative in order to simplify the analysis of the procedure [20, 66]. The updated snapshot matrices for each of the variables $\mathbf{S}_1, \mathbf{S}_2, \mathbf{S}_3$ are treated separately, but in an identical manner. Thus, the subscripts are omitted and the details are provided for a general snapshot matrix \mathbf{S} .

A “thin” singular value decomposition (SVD) of the snapshot matrix \mathbf{S} is performed

$$\mathbf{S} = \widetilde{\Theta} \Sigma \widetilde{\Psi}^T, \quad (13)$$

where $\Sigma = \text{diag}(\sigma_1, \dots, \sigma_M)$ is a $M \times M$ diagonal matrix containing the singular values arranged in decreasing order, $\sigma_1 \geq \sigma_2 \dots \geq \sigma_M$. $\widetilde{\Theta}$ and $\widetilde{\Psi}$ are unitary matrices of dimension $N \times M$ and $M \times M$, and containing the orthonormal left and right singular vectors of \mathbf{S} respectively, given by

$$\mathbf{S}\mathbf{S}^T \theta_n = (\sigma_n)^2 \theta_n, \quad \mathbf{S}^T \mathbf{S} \psi_n = (\sigma_n)^2 \psi_n, \quad 1 \leq n \leq M.$$

The columns θ_n of the matrix $\widetilde{\Theta}$ are also ordered corresponding to the singular values σ_n and these provide the desired basis vectors (or empirical modes) for the solution snapshot vector \mathbf{v} . This follows directly from eq. (13), as every column of the snapshot matrix \mathbf{S} lies in the range space of $\widetilde{\Theta}$, *i.e.* every solution snapshot vector can be represented as $\mathbf{v}^n = \bar{\mathbf{v}} + \widetilde{\Theta} \mathbf{c}$ for some vector \mathbf{c} . As a consequence of this property of the SVD, a lower dimensional (reduced order) approximation can be obtained by choosing a small number, $m \ll M$, of the leading empirical modes as the set of basis vectors. Let Θ denotes the matrix of the first m columns of $\widetilde{\Theta}$, then the high-fidelity solution \mathbf{y}^n at time t^n has the reduced order representation \mathbf{z}^n when projected onto the space of POD modes,

$$\mathbf{y}^n \approx \bar{\mathbf{y}} + \Theta \mathbf{z}^n = \bar{\mathbf{y}} + \sum_{i=1}^m z_i^n \theta_i. \quad (14)$$

Although the POD basis provides an optimally approximate representation of the snapshot space, some information is lost due to the inexactness of eq. (14). However, a desired level of accuracy, τ_{POD} can be obtained by choosing a truncation number m such that the following condition is satisfied: $\left(\sum_{i=m+1}^M \sigma^i / \sum_{i=1}^M \sigma^i\right) \leq \tau_{POD}$.

In traditional Galerkin/POD approach, a reduced order model for the time evolution of the state vectors is obtained by projecting the original high-dimensional model onto the reduced space spanned by the POD empirical modes. Returning to the high-fidelity SWE model in eq. (9), let $\mathbf{z} = (\mathbf{z}_1^T, \mathbf{z}_2^T, \mathbf{z}_3^T)^T \in \mathbb{R}^{m_1+m_2+m_3}$ denote the projected coordinates where m_1, m_2, m_3 are the POD truncation levels of the three state vectors. Also, define a global basis $\Theta = \text{diag}(\Theta_1, \Theta_2, \Theta_3)$ as a block-diagonal matrix. Using the representation given by eq. (14) in the high-fidelity, fully discrete, nonlinear system (12) and performing a standard Galerkin projection yields a reduced system of equations

$$\Theta^T \mathbf{R}^{n+1}(\bar{\mathbf{y}} + \Theta \mathbf{z}^{n+1}) = 0. \quad (15)$$

The system of m equations for the evolution of the POD coefficients \mathbf{z} , given by eq. (15), is a reduced order approximation of the high-fidelity system of $3N$ equations, given by eq. (12), and the full order solution can be recovered using eq. (14). In the numerical experiments below, eq. (15) will be referred to as the NPOD (Nonlinear POD) ROM. Due to the presence of nonlinearities, the NPOD model may still be slow, since the evaluation procedure scales like the fine dimension. Several *hyper-reduction* (approximation of the nonlinearity in a reduced space) strategies have been proposed to recover the lost efficiency [33, 67]. Note, that unlike the alternating direction implicit (ADI) scheme considered in [18], our fine-scale approximation involves non-polynomial nonlinear terms due to the bottom roughness parametrization and stabilization.

4. RBF-POD reduced order model formulation

In this section, we introduce the fundamental framework for approximating the time evolution of the coefficients of the POD expansion via kernel-based approximation schemes. The striking feature underlying this approach is that the construction of the kernel-based interpolation framework is independent of the POD-based reduced basis representation of the snapshot space.

4.1. Remarks on reproducing kernel Hilbert spaces

The problem of multivariate scattered data interpolation is stated as: given a set of N_d distinct points $\{\mathbf{x}_i \in \mathbb{R}^d, i = 1, 2, \dots, N_d\}$, and a set of N_d real numbers, $\{f_i, i = 1, 2, \dots, N_d\}$, find a continuous function $F(\mathbf{x})$ that satisfies $F(\mathbf{x}_i) = f_i, \forall i = 1, 2, \dots, N_d$. We employ radial basis function (RBF) interpolation for determining the function $F(\mathbf{x})$.

A function $\Psi : \mathbb{R}^d \rightarrow \mathbb{R}$ is called radial if for each $\mathbf{x} \in \mathbb{R}^d$, $\Psi(\mathbf{x}) = \phi(\|\mathbf{x}\|)$, where $\phi : [0, \infty) \rightarrow \mathbb{R}$ is an univariate function often termed as the radial basis kernel and $\|\cdot\|$ represents the Euclidean norm. Given the set of scattered centers $\mathbf{x}_i, i = 1, \dots, N_d$, a RBF interpolant

is defined as the linear combination of N_d instances of a chosen radial basis function ϕ , that are translated about the centers and has the form

$$F(\mathbf{x}) = \sum_{j=1}^{N_d} \alpha_j \phi(\|\mathbf{x} - \mathbf{x}_j\|), \quad (16)$$

where $\|\mathbf{x} - \mathbf{x}_j\|$ is the Euclidean distance between the observation point \mathbf{x} and the center \mathbf{x}_j . The unknown coefficients $\alpha_j, j = 1, 2, \dots, N_d$ are determined by solving a symmetric system of linear equations of order N_d generated by the interpolation conditions,

$$f_i = F(\mathbf{x}_i) \equiv \sum_{j=1}^{N_d} \alpha_j \phi(\|\mathbf{x}_i - \mathbf{x}_j\|), \quad (17)$$

where $\|\cdot\|$ denotes the Euclidean norm. The linear system may be written in the matrix form $\mathbf{A}\boldsymbol{\alpha} = \boldsymbol{\gamma}$, where $\boldsymbol{\alpha} = [\alpha_1, \alpha_2, \dots, \alpha_{N_d}]^T$, $\boldsymbol{\gamma} = [f_1, f_2, \dots, f_{N_d}]^T$ and

$$\mathbf{A} = [A_{ij}] = [\phi(\|\mathbf{x}_i - \mathbf{x}_j\|)]. \quad (18)$$

Such a system, admits a unique solution if the kernel is strictly positive definite. Otherwise, for conditionally positive definite functions, we need to add a polynomial term to make the problem well-posed [68, 69]. We now introduce the so-called reproducing kernel Hilbert spaces (RKHS) useful for studying later greedy algorithms and convergence results [58, 70].

Let us assume $\Phi : \Omega \times \Omega \rightarrow \mathbb{R}$ denotes a continuous, symmetric, and strictly positive definite kernel on a compact set, $\Omega \subset \mathbb{R}^d$. Let $V_\Omega = \text{span}\{\Phi(\cdot, \mathbf{x}) : \mathbf{x} \in \Omega\}$ denote the vector space spanned by all functions $\Phi(\cdot, \mathbf{x})$, which can be equipped with the natural inner product

$$\left(\sum_{j=1}^{N_d} \alpha_j \Phi(\cdot, \mathbf{x}_j), \sum_{k=1}^{N_l} \beta_k \Phi(\cdot, \tilde{\mathbf{x}}_k) \right)_\Phi := \sum_{j=1}^{N_d} \sum_{k=1}^{N_l} \alpha_j \beta_k \Phi(\mathbf{x}_j, \tilde{\mathbf{x}}_k). \quad (19)$$

It can be seen that Φ is the reproducing kernel of V_Ω with respect to the inner product $(\cdot, \cdot)_\Phi$ *i.e.* for each symmetric, positive definite Φ there is a unique such space with the reproducing property

$$(f, \Phi(\cdot, \mathbf{x}))_\Phi = f(\mathbf{x}), \quad \forall f \in V_\Omega, \mathbf{x} \in \Omega. \quad (20)$$

The closure of V_Ω yields a Hilbert space, induced by the reproducing kernel Φ over Ω , which is known as the reproducing kernel Hilbert space (RKHS) or the native Hilbert space to Φ and will be denoted by $\mathcal{N}_\Phi(\Omega)$.

Let $X = \{\mathbf{x}_1, \dots, \mathbf{x}_{N_d}\} \subset \Omega$ be a finite discrete subset and $\eta_j \in V_X := \text{span}\{\Phi(\cdot, \mathbf{x}) : \mathbf{x} \in X \subset \Omega\}$ denote the cardinal functions, also known as the Lagrangian basis, *i.e.* η_j satisfies $\eta_j(\mathbf{x}_k) = \delta_{jk}$. Then the interpolant given by eq. (16) can also be represented by

$$F(\mathbf{x}) = \sum_{j=1}^{N_d} f(\mathbf{x}_j) \eta_j. \quad (21)$$

Therefore, using the reproducing kernel property of eq. (20) and the cardinal representation in eq. (21), the interpolation error for a function $f \in \mathcal{N}_\Phi(\Omega)$ can be expressed as

$$f(\mathbf{x}) - F(\mathbf{x}) = \left(f, \Phi(\cdot, \mathbf{x}) - \sum_{j=1}^{N_d} \eta_j(\mathbf{x}) \Phi(\cdot, \mathbf{x}_j) \right)_\Phi. \quad (22)$$

Applying the Cauchy-Schwarz inequality to (22) leads to

$$|f(\mathbf{x}) - F(\mathbf{x})| \leq P_X(\mathbf{x}) \|f\|_\Phi, \quad (23)$$

where $P_X(\mathbf{x})$ denotes the power function (see [71], 11.2) which takes the explicit form

$$P_X^2(\mathbf{x}) := \left\| \Phi(\cdot, \mathbf{x}) - \sum_{j=1}^{N_d} \eta_j(\mathbf{x}) \Phi(\cdot, \mathbf{x}_j) \right\|_\Phi^2 \quad (24a)$$

$$= \Phi(\mathbf{x}, \mathbf{x}) - 2 \sum_{j=1}^{N_d} \eta_j(\mathbf{x}) \Phi(\mathbf{x}, \mathbf{x}_j) + \sum_{j,k=1}^{N_d} \eta_j(\mathbf{x}) \eta_k(\mathbf{x}) \Phi(\mathbf{x}_j, \mathbf{x}_k) \quad (24b)$$

$$= \Phi(\mathbf{x}, \mathbf{x}) - \mathbf{b}(\mathbf{x})^T \mathbf{A} \mathbf{b}(\mathbf{x}). \quad (24c)$$

As can be seen in eq. (24a), the power function is essentially the norm of the pointwise error functional, and it can be computed numerically as a quadratic form given by eq. (24b) using the Lagrange basis. The power function can also be evaluated using the alternate representation given by eq. (24c), where \mathbf{A} is the interpolation matrix as defined in eq. (18) and $\mathbf{b}(\mathbf{x}) = [\Phi(\mathbf{x}, \mathbf{x}_1), \dots, \Phi(\mathbf{x}, \mathbf{x}_{N_d})]^T$. It can be readily observed from eq. (24a) that whenever Φ is a strictly positive definite kernel, *i.e.*, \mathbf{A} is a positive definite matrix, then the power function satisfies the bounds

$$0 \leq P_X(\mathbf{x}) \leq \sqrt{\Phi(\mathbf{x}, \mathbf{x})}. \quad (25)$$

Moreover, if $X \subseteq Y$ are two point sets in Ω , then the associated power functions satisfy the following necessary minimization property

$$P_X(\mathbf{x}) \geq P_Y(\mathbf{x}), \quad \mathbf{x} \in \Omega. \quad (26)$$

The remarks above are meaningful for introducing greedy methods for our problem, as done in the next subsections.

4.2. RBF approximation of the reduced coefficients

In this work, the temporal dynamics of the governing system of equations is approximated using multidimensional RBF interpolation over the set of projected high-fidelity snapshots. For simplicity, it is assumed that the time evolution of the projected reduced snapshots \mathbf{z} can be represented as a semi-discrete dynamical system,

$$\dot{\mathbf{z}} = \mathbf{f}(\mathbf{z}, t), \quad (27)$$

where all the information about the temporal dynamics including the SUPG stabilization and other nonlinear terms are embedded in $\mathbf{f}(\mathbf{z}, t)$. Introducing a first-order time discretization, the reduced solution at time level $n + 1$ can be obtained by

$$z_j^{n+1} = z_j^n + \Delta t^n f_j(\mathbf{z}^n), \quad n \in \{0, 1, \dots, M - 1\}, j \in \{1, 2, \dots, m\}, \quad (28)$$

subject to the initial condition

$$\mathbf{z}^0 = \Theta^T (\mathbf{v}^0 - \bar{\mathbf{v}}). \quad (29)$$

In general, the NPOD reduced model given by eq. (15) can be recast in a similar discrete dynamical system form that is based on a Galerkin projection framework. In the proposed POD-RBF NIROM framework, the time derivatives $f_j (j = 1, \dots, m)$ in eq. (28) are approximated using RBF interpolation. This approach is a generalization of the strategy adopted in [49], where RBF interpolation was employed to approximate the evolution of the reduced solution using the direct iteration scheme $\mathbf{z}^{n+1} = \tilde{\mathbf{f}}(\mathbf{z}^n)$. The approach in eq. (28) allows us to isolate the error in the discrete approximation of the time derivative of the reduced solution from the overall error of the reduced order model. The numerical experiments in this paper have been obtained with a first-order time discretization, as shown in eq. (28), but the application of higher order discretization schemes would be straightforward.

There are many kernels available in RBF literature which differ in terms of smoothness. In the context of the shallow water applications, kernels with limited regularity may be preferable, and this motivates the choice of the strictly positive definite Matérn C^0 kernel, given by $\phi(r) = e^{-cr}$. The constant c is referred to as the shape parameter of the corresponding RBF and can affect the accuracy of the fit. For further details about its tuning, we refer the reader to [69].

Let F_j denote a RBF interpolant approximating the time derivative function f_j for a single POD coefficient z_j^{n+1} at time level $(n + 1)$, defined by a linear combination of N_i instances of a radial basis function ϕ . Then it assumes the form,

$$F_j(\mathbf{z}) = \sum_{k=1}^{N_i} \alpha_{j,k} \phi(\|\mathbf{z} - \hat{\mathbf{z}}_k\|), \quad j = 1, \dots, m, \quad (30)$$

where $\{\widehat{\mathbf{z}}_k \mid k = 1, \dots, N_i\}$ denotes the set of ‘‘centers’’ or trial points and $\alpha_{j,k}$ ($k = 1, \dots, N_i$) is the unknown coefficient corresponding to the k^{th} center for the j^{th} POD coefficient. The coefficients $\alpha_{j,k}$ are computed by enforcing the interpolation function F_j to exactly match the time derivative of the POD coefficients at N_e test points ($N_e \geq N_i$), that is,

$$g_{j,n} \equiv \frac{z_j^{n+1} - z_j^n}{\Delta t^{n+1}} = \sum_{k=1}^{N_i} \alpha_{j,k} \phi(\|\mathbf{z}^n - \widehat{\mathbf{z}}_k\|), \quad n = 1, \dots, N_e; j = 1, \dots, m. \quad (31)$$

In this work, the set of centers and the test points have been identically chosen from the set of projected snapshots as $\{\mathbf{z}^l \mid l = 0, \dots, M-1\}$ such that $N_i = N_e = M$. The time derivative functions are assumed to be independent of the time step which leads to a symmetric system of M equations to obtain the unknown coefficients, $\alpha_{j,k}$ for $k \in 0, \dots, M-1$ and $j = 1, \dots, m$. Thus, for $j = 1, \dots, m$, the problem reduces to solving a system of M linear equations

$$\mathbf{A}^j \boldsymbol{\alpha}^j = \mathbf{g}^j, \quad (32)$$

where

$$[A_{n,k}^j] = [\phi(\|\mathbf{z}^n - \mathbf{z}^k\|)], \quad n, k = 0, \dots, M-1, \\ \boldsymbol{\alpha}^j = [\alpha_{j,0}, \alpha_{j,1}, \dots, \alpha_{j,M-1}]^T, \quad \mathbf{g}^j = [g_{j,0}, g_{j,1}, \dots, g_{j,M-1}]^T.$$

The coefficients $\boldsymbol{\alpha}^j$ define a unique RBF interpolant which can then be used to approximate eq. (28) and generate a non-intrusive model for the evolution of the reduced solution as

$$\tilde{z}_j^{n+1} = \tilde{z}_j^n + \widetilde{\Delta t}^n F_j(\tilde{\mathbf{z}}^n), \quad n \in \{0, \dots, M-1\}; j \in \{1, \dots, m\}, \quad (33)$$

with an appropriate initial condition $\tilde{\mathbf{z}}(\cdot, 0) = \tilde{\mathbf{z}}^0$. We conclude by pointing out that, RBF tools are easy to implement in any dimensions, but their computational need might be prohibitive if a large number of centers is involved. Thus we now present three algorithms devoted to selecting an optimal (minimal) number of nodes and their location.

4.3. Optimal distribution of RBF interpolation points

A key aspect of finding an efficient sparse approximation using a radial basis kernel is the concept of m -term approximation [72], which is basically a measure of how accurately a function from a given function space can be approximated by the linear combination of m functions belonging to a subset of the same space. This leads to the challenge of finding methods and algorithms that determine the best or near-best m -term approximations. In the context of RBF interpolation several adaptive schemes have been proposed for the selection

of an optimal set of centers like thinning algorithms [73], greedy algorithms, and k-mean clustering methods [74, 75, 76]. In this work, we consider methods belonging to the family of greedy algorithms, which have been demonstrated to yield near-optimal m -term approximations under various conditions [77, 78, 79, 80]. The “greedy” aspect of these algorithms has its foundation in a greedy step, which determines the next center to be added to the existing set of chosen centers according to certain minimizing criteria involving residuals or power functions. Some approximation and convergence results have been established for greedy algorithms in general spaces, e.g. Hilbert [72] or Banach spaces [81].

4.3.1. p -greedy algorithm

It can be observed from eq. (23), that the power function helps us to estimate the interpolation error by allowing us to decouple the effects due to the values of the data function f from the effects of the kernel Φ and the location of the centers $\{\mathbf{x}_j\}_{j=1}^{N_d}$. This crucial observation, along with the error bounds (25), and the minimization property (26) were the key ingredients used by De Marchi *et al.* [57] to develop the p -greedy algorithm as a method to iteratively obtain a near-optimal set of center locations that are independent of the data values.

Let $X = \{\mathbf{z}_i \mid 0 \leq i \leq M\}$ be the set of all the projected high-fidelity snapshots or centers for the radial basis kernel. The first selected center is given by $\mathbf{z}_1 = \operatorname{argmax}_{\mathbf{z}_i \in X} \{\Phi(\mathbf{z}_i, \mathbf{z}_i)\}$. Let us assume that after k greedy iterations, the set of selected centers is given by X_k such that $\dim X_k = k$. In the $(k + 1)^{th}$ iteration, the power function is evaluated at each of the remaining centers in $X \setminus X_k$, and the worst approximated center \mathbf{z}_{k+1} *i.e.* the center at which the power function attains the maximum value, is selected to enrich the existing set of centers. This process continues until the maximum value of the power function drops below a chosen tolerance τ_p . The p -greedy algorithm has been summarized in Algorithm 1 and its efficiency in the context of multidimensional RBF interpolation is studied through numerical examples in Section 5.2.

Remark. The main advantage of the p -greedy approach is that the set of reduced centers is computed only one time, independently from the number of modes. The main drawback is that this approach only accounts for one term in the upper bound given by eq. (23), indeed, we are not looking at the function values. To partially overcome this, we drive our attention

towards the f -greedy schemes.

Algorithm 1: p-greedy algorithm for selecting optimal set of RBF centers

Result: \tilde{X} : Optimal set of RBF centers
Input : $X = \{\mathbf{z}_1, \mathbf{z}_2, \dots, \mathbf{z}_M\}$, $M > N_{max}$

- 1 Initial center: $\mathbf{z}_1 = \operatorname{argmax}_{\mathbf{z}_i \in X} \{\Phi(\mathbf{z}_i, \mathbf{z}_i)\}$
- 2 **while** $\max\{P_{X_k}(\mathbf{z}_i)\} > \tau_p$ & $N_k < N_{max}$ **do**
- 3 Compute $P_{X_k}(\mathbf{z}_i)$, $\forall \mathbf{z}_i \in X \setminus X_k$
- 4 Let $\mathbf{z}_{k+1} = \operatorname{argmax}_{\mathbf{z}_i \in X \setminus X_k} \{P_{X_k}(\mathbf{z}_i)\}$
- 5 $X_{k+1} \leftarrow X_k \cup \{\mathbf{z}_{k+1}\}$
- 6 Re-compute RBF system: $\mathbf{F}_{k+1}, \mathbf{A}_{k+1}$
- 7 **end**

4.3.2. f -greedy algorithm

The p -greedy algorithm is designed to primarily capture the effect of the radial kernel and the location of the center points on the interpolation error, and this is expected to be helpful when the variation in the values of the interpolated function is relatively regular. In the context of RBF-based NIROMs, the underlying function is the time derivative of the solution snapshots, projected on to the POD space. Depending on the characteristics of the shallow water flow problem being studied, the projected snapshots can have highly nonlinear temporal evolution patterns. In order to capture the trend in the time derivative function, we have also studied a residual-based f -greedy algorithm.

The idea of iteration on residuals leading to the scalar f -greedy algorithm, was introduced by Schaback and Wendland in [58], where they also provided a convergence proof using the orthogonality relation,

$$(F, f - F)_\Phi = 0, \quad \forall f \in \mathcal{N}_\Phi. \quad (34)$$

The orthogonality property is a direct consequence of the fact that the RBF interpolant F has the minimal norm among all functions in the native space \mathcal{N}_Φ that interpolate f on X . The orthogonality property allows the following Pythagorean splitting of the “energy” of the function f using the native norm

$$\|f\|_\Phi^2 = \|f - F\|_\Phi^2 + \|F\|_\Phi^2. \quad (35)$$

A recursive application of (35) easily shows that $\lim_{k \rightarrow \infty} \|f - F_k\|_\Phi = 0$, where F_k is the k -term interpolant, and this forms the key ingredient of the scalar f -greedy algorithm. In the $(k + 1)^{th}$ iteration, the absolute value of the k^{th} function residual *i.e.* the difference between the data value f and the k -term interpolant function F_k , is computed for each center remaining in the pool of unused centers $X \setminus X_k$. Then, the center \mathbf{z}_{k+1} at which the maximum error of the k^{th} function residual occurs, is added to the existing set of centers *i.e.* $X_{k+1} = X_k \cup \{\mathbf{z}_{k+1}\}$.

In the context of our interpolation problem, the function residual is vector valued, *i.e.* $|f - F_k| \in \mathbb{R}^m$ where $m = m_1 + m_2 + m_3$ is the total number of POD modes for all the solution components. However, the interpolation conditions (31) are applied individually for each mode to generate independent modal interpolants. Hence, transferring the scalar *f-greedy* algorithm directly to the vectorial case by a mode-wise application results in m near-optimal sets of centers $X_k^j (j = 1, \dots, m)$. Despite the simplicity of this approach, in the absence of a mechanism to enforce a coordinated choice over all m modes the resulting sets of centers X_k^j might only have very few points in common or even be pairwise disjoint. Then, assuming that the sets of centers have approximately the same number of elements (*i.e.* $|X^j| \approx |X^i|, j \neq i$), the kernel has to be evaluated at roughly $m|X^j|$ different centers and the cost of evaluation in the online computation scales with a factor of m . Moreover, the offline computational cost also scales with a factor of m in the worst case, which can lead to substantially longer times for large training sets of snapshots.

To avoid this additional computational overhead, an alternative strategy is proposed to identify a subset of modes ($\ll m$) for which a unified set of centers X can be determined using a *f-greedy* approach. The “energy” content of individual modes is computed as

$$\hat{e}_j^i = \sum_{k=0}^{M-1} \left(\left. \frac{dz_{k,j}}{dt} \right|_i \right)^2, \quad (36)$$

where $z_{k,j} \big|_i$ is the j^{th} mode of the k^{th} center, $\mathbf{z}_k = [z_{k,0}, z_{k,1}, \dots, z_{k,m}]^T$ for the i^{th} solution component. The modes are arranged in the descending order of energy content and then, the set of the most significant modes for each component, $L_i = \{j \mid j \leq m_i^j \ll m_i\}$ are identified by selecting a desired fraction τ_{greedy} such that

$$\left(\sum_{j=0}^{j=m_i^j} \hat{e}_j^i \right) / \left(\sum_{j=0}^{j=m_i} \hat{e}_j^i \right) \leq \tau_{\text{greedy}}. \quad (37)$$

Alternatively, a suitable subset of modes L_i can also be identified visually by studying the variation in the time derivative functions dz/dt for individual modes, and selecting the modes for each solution component with the highest amplitude of variations. Both of these procedures have been demonstrated in the numerical results. A combined set of modes $L = L_1 \cup L_2 \cup L_3$ is used to iteratively apply the *f-greedy* algorithm, such that for a particular mode in each greedy iteration, the center at which the residual error is maximum is chosen to enrich the existing set of centers. This process continues until the absolute value of the difference between the maximum modal residual errors in two successive iterations becomes less than a chosen absolute tolerance τ_f . The initial center is defined by $\mathbf{z}_1 = \operatorname{argmax}_{\mathbf{z}_i \in X} \{|f_j(\mathbf{z}_i)|\}$ where $f_j(\mathbf{z}_i)$ denotes the j^{th} component of the data function evaluated at the center point, \mathbf{z}_i and j denotes the first mode in L . The greedy iterative process is then repeated for every mode in the set of selected significant modes L and the entire procedure is presented in Algorithm 2. It is worth mentioning that a vector variant of the *f-greedy* algorithm was also studied, in

which, the center at which the discrete l^2 norm of the function residual was maximum, was chosen to enrich the existing set of centers. However, this strategy was found ineffective for any of the shallow water flow examples considered.

Algorithm 2: f -greedy algorithm for selecting optimal set of RBF centers

Result: \tilde{X} : Optimal set of RBF centers
Input : $X = \{\mathbf{z}_1, \mathbf{z}_2, \dots, \mathbf{z}_M\}$, $M > N_{max}$
 $L = \{j | j \leq m_i^j\}$, $|L| \ll m$: List of selected significant modes

- 1 Initial center: $\mathbf{z}_1 = \operatorname{argmax}_{\mathbf{z}_i \in X} \{|f_j(\mathbf{z}_i)| : j \text{ is the first mode in } L\}$
- 2 **for** j in L **do**
- 3 **do**
- 4 Compute $\xi_{X_k}^j(\mathbf{z}_i) = |f_j(\mathbf{z}_i) - F_{k,j}(\mathbf{z}_i)|$, $\forall \mathbf{z}_i \in X \setminus X_k$
- 5 Set $\mathbf{z}_{k+1} = \operatorname{argmax}_{\mathbf{z}_i \in X \setminus X_k} \{\xi_{X_k}^j(\mathbf{z}_i)\}$
- 6 $X_{k+1} \leftarrow X_k \cup \{\mathbf{z}_{k+1}\}$
- 7 Re-compute RBF system: $\mathbf{F}_{k+1}, \mathbf{A}_{k+1}$
- 8 **while** $\left| \max\{\xi_{X_k}^j\} - \max\{\xi_{X_{k-1}}^j\} \right| > \tau_f \ \& \ N_k < N_{max}$
- 9 **end**

4.3.3. psr -greedy algorithm

In this work, a new strategy called the power-scaled greedy or psr -greedy algorithm has been developed to construct NIROMs for problems where both the variation in data values as well as the dependence on the kernel functions are considered equally significant.

A scalar fp -greedy algorithm was proposed in [82], where a ratio of the function residual and the power function is adopted as the selection metric, thus minimizing the native RKHS norm $\|f - F_k\|_{\Phi}$ in each greedy step. Essentially this scalar variant weighs the residual error at the center being examined with how effectively the considered center is already contained in the current set of centers. A direct application of the scalar algorithm to the vectorial setting suffers from the same computational disadvantages that were discussed in the context of the f -greedy algorithm. A vectorized strategy named the Vectorial Kernel Orthogonal Greedy algorithm (VKOGA, [70]) was suggested which attempts to extend the scalar orthogonality property of RBF interpolants (see (34)) by introducing the concept of a vectorial gain function. Then a greedy maximization of the gain function leads to an iterative addition of the largest possible “gain” in approximation with respect to the native space norm.

The psr -greedy algorithm proposed here uses a strategy similar to the f -greedy algorithm (see eq. (36) and Algorithm 2) to select a subset of POD modes corresponding to each solution component for which the modal residual computations are carried out. The novelty lies in the minimization of the product of the power function and the modal function residual in order to greedily select the worst approximated centers. Thus it aims to simultaneously eliminate the error introduced by both the kernel as well as the function variations. The initial center is defined by $\mathbf{z}_1 = \operatorname{argmax}_{\mathbf{z}_i \in X} \{\Phi(\mathbf{z}_i, \mathbf{z}_i) |f_j(\mathbf{z}_k)|\}$ where j corresponds to the first mode in L . This is summarized in Algorithm 3.

Remark. The development of the *psr-greedy* scheme is driven by the observation that dividing any quantity by the power function, $P_X(\mathbf{x}) \ll 1$, turns out to be extremely unstable. Indeed, if two centers are close to each other such that $\|\mathbf{x}_1 - \mathbf{x}_2\| \rightarrow 0$, then the power function is almost zero *i.e.* $P_X(\mathbf{x}_2) \rightarrow 0$, if $\mathbf{x}_1 \in X$. Also, we observe that multiplying (23) by the power function and taking into account (25), we have

$$P_X(\mathbf{x})|f(\mathbf{x}) - F(\mathbf{x})| \leq P_X^2(\mathbf{x})\|f\|_{\Phi} \leq \|f\|_{\Phi}, \quad (38)$$

provided that $\Phi(\mathbf{x}, \mathbf{x}) = 1$, which is true for the Matérn C^0 kernel (as well as for some other p.d. kernels like the Gaussian). This provides an empirical motivation for the effectiveness of our approach.

Moreover, as it will become evident in the experiments, the centers selected using the *f-greedy* algorithm may exhibit a strong clustering pattern. This means that where the function has high variations owing to nonlinearities, the *f-greedy* may suffer from oversampling, whereas the centers where steep gradients may still be present but the nonlinearities are less dominant, may be under represented. The *psr-greedy* is able to overcome this sub-optimal behavior by the application of the power function as a variable scaling factor and by using a suitable tolerance τ_{psr} . The power function increases the relative importance of centers in under-sampled regions, while the tolerance factor ensures that all of the relevant nonlinear features are suitably represented. This may explain the redistribution of the clustering patterns using the *psr-greedy* algorithm.

Algorithm 3: psr-greedy algorithm for selecting optimal set of RBF centers

Result: \tilde{X} : Optimal set of RBF centers
Input : $X = \{\mathbf{z}_1, \mathbf{z}_2, \dots, \mathbf{z}_M\}$, $M > N_{max}$
 $L = \{j \mid j \leq m_i^j\}$, $|L| \ll m$: List of selected significant modes

- 1 Initial center: $\mathbf{z}_1 = \operatorname{argmax}_{\mathbf{z}_i \in X} \{\Phi(\mathbf{z}_i, \mathbf{z}_i) | f_j(\mathbf{z}_k) | : j \text{ is the first mode in } L\}$
- 2 **for** j in L **do**
- 3 **do**
- 4 Compute $\xi_{X_k}^j(\mathbf{z}_i) = P_{X_k}(\mathbf{z}_i) |f_j(\mathbf{z}_i) - F_{k,j}(\mathbf{z}_i)|$, $\forall \mathbf{z}_i \in X \setminus X_k$
- 5 Set $\mathbf{z}_{k+1} = \operatorname{argmax}_{\mathbf{z}_i \in X \setminus X_k} \{\xi_{X_k}^j(\mathbf{z}_i)\}$
- 6 $X_{k+1} \leftarrow X_k \cup \{\mathbf{z}_{k+1}\}$
- 7 Re-compute RBF system: $\mathbf{F}_{k+1}, \mathbf{A}_{k+1}$
- 8 **while** $|\max\{\xi_{X_k}^j\} - \max\{\xi_{X_{k-1}}^j\}| > \tau_{psr} \ \& \ N_k < N_{max}$
- 9 **end**

The straightforward implementation of the greedy algorithms using the standard basis of translates $\{\Phi(\mathbf{z}_1, \cdot), \dots, \Phi(\mathbf{z}_M, \cdot)\}$ or using the Lagrange basis functions $\eta_j, j = 1, \dots, M$ with the property $\eta_j(\mathbf{z}_i) = \delta_{ij}$, may pose severe computational challenges. This is because every greedy iteration involves potentially ill-conditioned kernel matrices and requires re-computing the entire set of RBF coefficients. In this work, we have adopted the fairly general Newton basis approach formulated in [83] for the p-greedy iterations. This approach was

extended to the multidimensional setting for VKOGA in [84], and has been applied here, with suitable modifications, for the modal residual computations required in the f-greedy and psr-greedy iterations.

4.4. Combined RBF-POD reduced order model

The key steps in the RBF-POD NIROM procedure are outlined below.

- (i) The high-fidelity snapshots $\mathbf{v}_i^1, \dots, \mathbf{v}_i^M$ for each component u_i are obtained by solving eq. (12), normalized and stored in \mathbf{S}_i .
- (ii) The truncated set of POD basis vectors Θ_i are obtained by performing a SVD of \mathbf{S}_i as given by eq. (13).
- (iii) The normalized high-fidelity snapshots are projected onto the space spanned by the POD basis to obtain the corresponding projected snapshots $\mathbf{z}_i^1, \dots, \mathbf{z}_i^M$ as defined by eq. (14).
- (iv) A subset of projected snapshots is selected using an appropriate greedy algorithm (Algorithms 1, 2 or 3) to define a near-optimal set of centers \tilde{X} for the RBF interpolant.
- (v) The RBF interpolants $F_j(\mathbf{z})$ for the modal time derivatives of the projected snapshots $\frac{d\mathbf{z}_j}{dt}$ is defined by solving the linear system of interpolation conditions, given by eq. (32), on the set of near-optimal centers \tilde{X} .
- (vi) The interpolants $F_j(\mathbf{z})$ are used in the RBF-POD NIROM equations, given by eq. (33), to advance the reduced solution in time for any new configuration queried by the application.

5. Numerical Results

Numerical tests have been conducted with different types of shallow water flow problems. To compare the performance of the POD-RBF NIROM with the nonlinear POD (NPOD) model, a riverine flow problem with moderately large degrees of freedom has been studied numerically, as discussed in Section 5.1. In Section 5.2, we consider two different flow regimes to evaluate the performance of the greedy algorithms. The first example represents tidal flow conditions in an urbanized bay, while the second example considers a different riverine flow with variable inflow boundary conditions. The bathymetry data in all of the examples were obtained from USACE Hydrographic surveys. All the bed topography measurements and water surface elevations were referenced with respect to the bathymetry data, following the NAVD88 convention.

For the purpose of demonstrating the efficiency of the model reduction methodology, only one well resolved high fidelity simulation has been used in the offline stage to generate the training data or snapshots. These snapshots have been used in the construction of the reduced order models, which have been employed to resolve the problems for different time step sizes in the online stage. In addition to comparing solution profiles, the approximation of overall

temporal dynamics is analyzed by comparing the weighted root mean square error (wRMSE), which is calculated separately for each component and each time step n by

$$wRMSE_j^n = \sqrt{\frac{\sum_{i=1}^N |y_{f,j,i}^n - y_{a,j,i}^n|^2}{N \sum_{i=1}^N |y_{f,j,i}^n + \text{offset}|^2}}. \quad (39)$$

In the above definition, $y_{f,j,i}^n$ denotes the high-fidelity model solution at the spatial node i for component $j \in \{1, 2, 3\}$, $y_{a,j,i}^n$ denotes the corresponding full order solution at the node i , reconstructed from the ROM solution (NIROM or NPOD) projected back onto the full mesh, and N represents the number of spatial nodes in the high-dimensional mesh. An offset = 0.0005 is used for the velocity variables and a zero offset is used for the depth. For ease of interpretation, we will focus on the primitive variables, \mathbf{h} , \mathbf{u}_x and \mathbf{u}_y . That is, $y_{f,1,i} = h_{f,i}$, $y_{f,2,i} = (u_x)_{f,i}$, and $y_{f,3,i} = (u_y)_{f,i}$.

Additionally, to compare the convergence behavior of the greedy NIROM strategies, a global measure of space-time approximation error is introduced as the space-time root mean square error (stRMSE). For any solution component, given a particular configuration of the NIROM, the stRMSE is computed as

$$stRMSE_j = \sqrt{\frac{\sum_{n=1}^M \sum_{i=1}^N |y_{f,j,i}^n - y_{a,j,i}^n|^2}{NM}}, \quad (40)$$

where M represents the total number of time steps in the online stage.

5.1. Comparison between NIROM and NPOD

5.1.1. Kissimmee River Example

The first numerical example involves the simulation of the hydrodynamic conditions along a stretch of the Kissimmee River near Fort Basinger in Florida, USA (see Fig. 1). The numerical model was obtained from the study [85] conducted to assess the expected inundation amounts associated with two different habitat restoration alternatives. In our simulation of the existing conditions configuration, the flow was primarily confined to the C-38 flood control drainage canal that is bounded upstream and downstream by water control structures of S-65C and S-65D, respectively. A high-fidelity hydrodynamic modeling of the river and the surrounding floodplain involved accurate representation of the bathymetry, multiple types of friction specification for the flood control channel and the overland vegetative floodplain, as well as accurate measurement of the discharge through the control structures. Additionally, accurate modeling of the tributary inflow, hydrodynamic conditions around the bridges (U.S. Highway 98 and CSX Railroad) as well as the floodplain discharges around 10 existing culverts along the U.S. Highway 98 causeway were necessary to determine the full range of

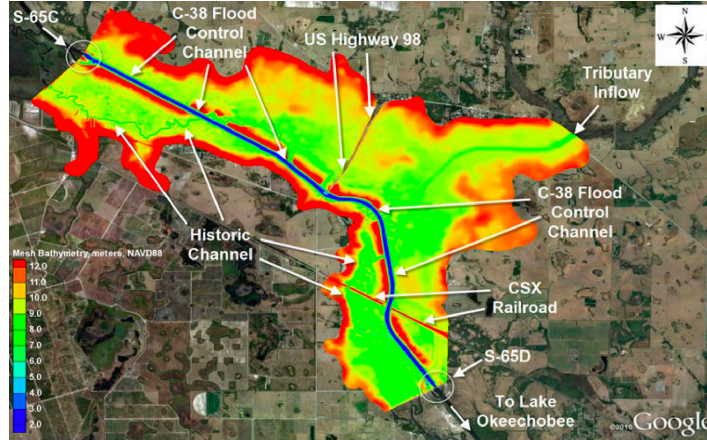


Figure 1: Kissimmee River

impacts associated with the existing conditions. Details can be found in McAlpin *et al.* [85].

A uniform structured triangular mesh consisting of $N = 108816$ nodes and 216676 elements was used. The simulation was carried out until $T = 4.5 \times 10^5$ seconds (≈ 5 days, 5 hours) with a linearly increasing time step ranging from $\Delta t = 5$ seconds to $\Delta t = 500$ seconds. A natural inflow boundary condition was specified at S-65C along with an outflow tailwater elevation at S-65D, and another natural velocity inflow condition was specified to simulate the tributary inflow. No flow boundary conditions were applied along the rest of the river and an initial water surface elevation for the entire domain was provided. Moreover, this example involves viscosity $\nu = 1.306 \times 10^{-5}$, Manning's roughness coefficient $n_{nm} = 0.03$ for the channelized areas, a submerged vegetation specification for overbank areas, and gravity $g = 9.81$.

In the offline stage, 2019 high-fidelity solution snapshots were collected. A subset of $M = 673$ snapshots was created by skipping over every 3 consecutive snapshots, which was used to generate the optimal POD space and subsequently the first 672 projected snapshots were used as center points to construct the RBF interpolant. The POD modes were truncated to the first 221, 317, and 315 modes for the primitive variables \mathbf{h} , \mathbf{u}_x , and \mathbf{u}_y respectively by selecting an error tolerance of $\tau = 10^{-4}$. The online simulations using the NIROM and NPOD reduced models were done with time steps identical to the full set of high-fidelity snapshots.

Figures 2 and 3 show the x-velocity solutions (left column) and the corresponding errors (right column) calculated using the RBF NIROM and the NPOD model respectively at time $t = 1.2995 \times 10^4$. The relative error 2-norm reported in Figures 2(b) and 3(b) were computed as the ratio of the l^2 norm of the absolute error with the l^2 norm of the true solution, and the NIROM can be

t_{HFM}	t_{NIROM}	t_{NPOD}
02 : 24 : 46	00 : 02 : 34	16 : 58 : 49
	(56.40×)	(0.14×)

Table 1: Computational times for the Kissimmee River example

seen to perform marginally better than the NPOD solution. However, the computational gain for the NIROM is significantly higher than the NPOD model as shown in Table 1, where the CPU time for each method has been reported for a simulation period of the first 24 hours of the original problem.

Figure 4a shows the wRMSE-norm with time for the velocity variables, u_x and u_y computed using both the reduced solutions while Figure 4b shows a similar comparison for the depth variable. The majority of the temporal dynamics are at the beginning of the simulation before the flow settles down to a steady state. Hence, the local extrema in the wRMSE plots for both the reduced order solutions occur at the early stages of the flow and accordingly the error profiles have been plotted for the first 200,000 seconds (≈ 55.5 hours). It can be observed that the NIROM produces a more robust and accurate approximation.

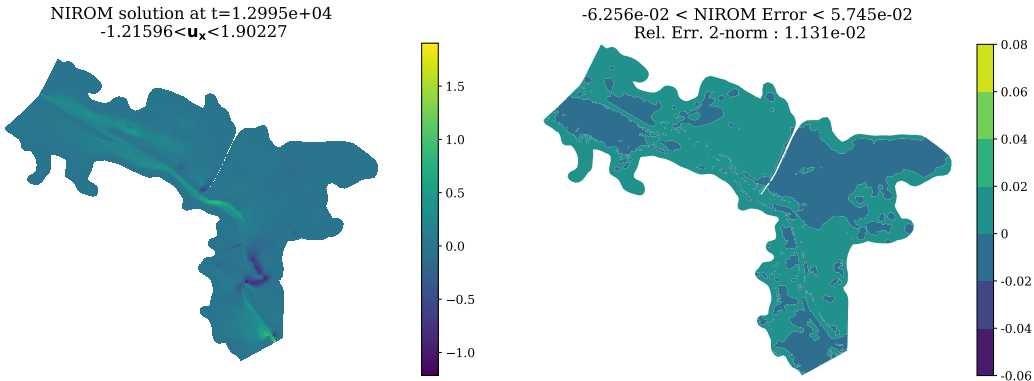


Figure 2: NIROM solution for the x-velocity (left column) and the error (right column) with respect to the true solution at $t = 1.2995 \times 10^4$ seconds.

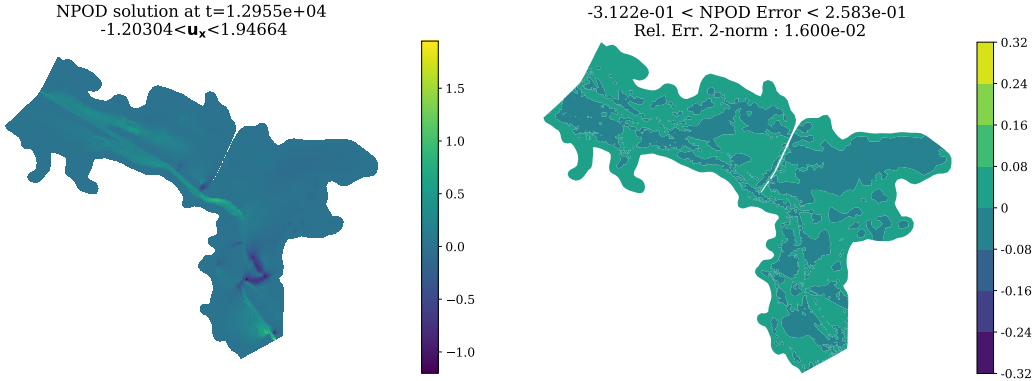


Figure 3: NPOD solution for the x-velocity (left column) and the error (right column) with respect to the true solution at $t = 1.2995 \times 10^4$ seconds.

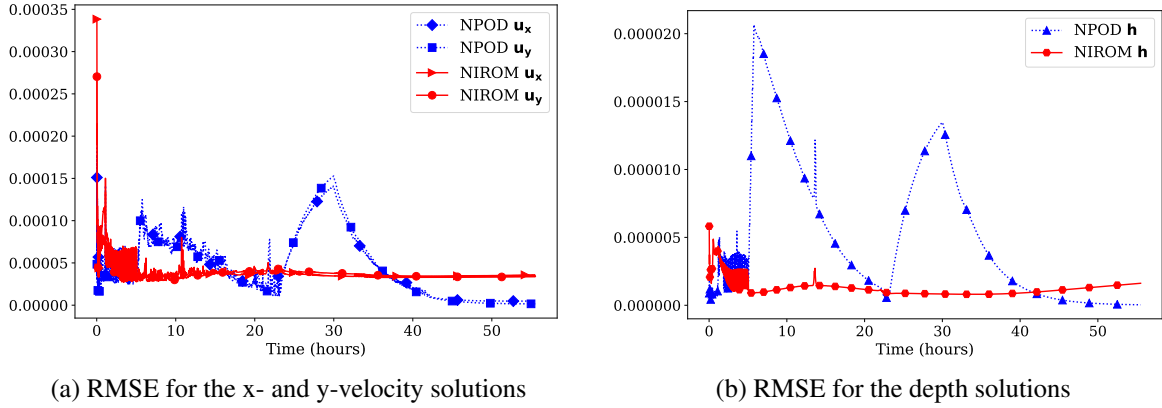


Figure 4: Comparison of the $wRMSE$ of the NIROM and NPOD reduced solutions for the Kissimmee River example

5.2. Performance of the greedy algorithms

In this section, numerical results are presented to comparatively evaluate the performance of the three different greedy strategies, described in Section 4.3, for the selection of an optimal set of RBF centers.

5.2.1. Red River Example

The first numerical example is an application of the 2D SWE to simulate riverine flow in a section of the Red River in Louisiana, USA (see Fig. 5).

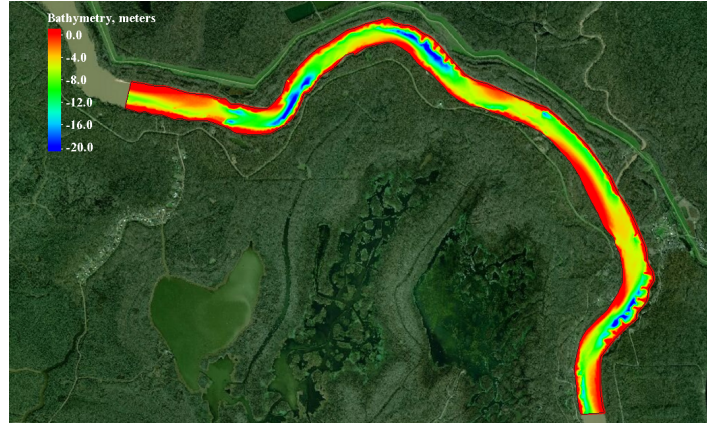


Figure 5: Red River

A uniform structured triangular mesh consisting of $N = 12291$ spatial nodes and 23316 elements was used. The simulation was carried out until $T = 60020$ seconds (16 hours, 40 minutes, and 20 seconds) with a time step of $\Delta t = 10$ seconds. A natural inflow velocity condition was specified upstream and a tailwater elevation boundary was specified downstream using hydrograph and bathymetry measurements obtained from USGS and USACE sources. No flow boundary conditions were applied along the banks of the river and an ini-

tial water surface elevation for the entire fluid flow domain was provided. A fluid viscosity $\nu = 1.139 \times 10^{-6}$, and Manning’s drag coefficient $n_{nm} = 0.025$ were also specified.

In the offline stage, a total of 6002 high-fidelity solution snapshots were collected. A subset of uniformly spaced 2001 snapshots, selected by skipping over every 3 consecutive snapshots, was used for computing the POD basis. Using a POD truncation error of $\tau = 0.01$, only the first 5, 221, and 213 POD modes were selected to construct the reduced basis space for the \mathbf{h} , \mathbf{u}_x , and \mathbf{u}_y components respectively. The online simulations using the different NIROM reduced models were carried out until $t = 9$ hours, with a time step of $\Delta t = 20$ seconds.

The subset of 2001 snapshots were projected onto the POD space to generate the set X of all the potential centers or data points available for the RBF interpolant. The p-greedy center points were selected using a tolerance $\tau_p = 0.10$, while the f-greedy and the psr-greedy centers were selected using tolerances $\tau_f = 0.11$ and $\tau_{psr} = 0.14$ respectively. The choice of the tolerances were driven by the need to generate sufficiently large sets of centers for effective comparison of the greedy NIROM solutions and numerical convergence studies.

L	\mathbf{h}			\mathbf{u}_x			\mathbf{u}_y		
	\mathbf{h}	\mathbf{u}_x	\mathbf{u}_y	\mathbf{h}	\mathbf{u}_x	\mathbf{u}_y	\mathbf{u}_x	\mathbf{u}_y	
	0			1			2	2	3
<i>f-greedy</i>	36	75	178	276	410	566	718	763	810
<i>psr-greedy</i>	22	65	147	278	441	516	673	766	914

Table 2: Number of centers selected using the f-greedy and the psr-greedy algorithms for the Red River example

As shown in the first row of Table 2, the initial set of modal residual computations for both the f-greedy and the psr-greedy algorithms were carried out by looping over the first two dominant modes for each of the projected solution components \mathbf{h} , \mathbf{u}_x , \mathbf{u}_y . Subsequently, further modal residual computations were done using the third mode of \mathbf{u}_x as well as the third and fourth modes of \mathbf{u}_y . Hence, the list of modes, as referenced in algorithms 2 and 3), was given by $L = \{0, 5, 226, 1, 6, 227, 7, 228, 229\}$. The second and third rows of Table 2 provide an account of the number of f-greedy and psr-greedy centers selected, respectively, at the end of each set of modal iterations.

The modal energy given by eq. (36) is distributed relatively evenly across the modes for the velocity components, which prevents an efficient truncation of modes as required by the f-greedy and the psr-greedy algorithms. In such cases, the modes may be manually selected to populate the list L by a visual analysis of the temporal evolution of the individual modes of the time derivative functions of each of the projected solution components. Figure 6 is a visualization of the most significant temporal dynamics for each of the solution components. This is captured by computing the modal l^2 -norm of the time derivative function, $\sum_{k=1}^{m_i} |dz_{i,k}^n/dt|^2$, for each of the projected solution components ($i = 1, 2, 3$). The irregular peaks in the visualization of the temporal dynamics signify non-trivial changes in the overall flow patterns, potentially induced by factors like the inflow and the discharge boundary conditions. A ma-

For objective of the greedy algorithms is to be able to efficiently capture these flow patterns with an optimal set of data points or centers.

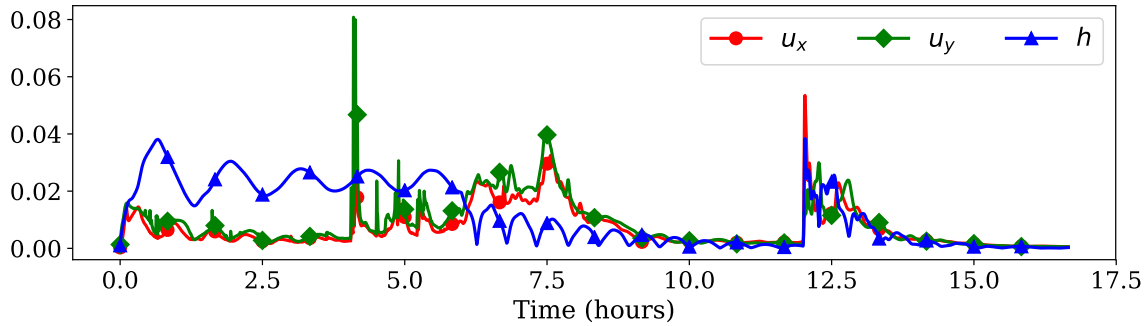
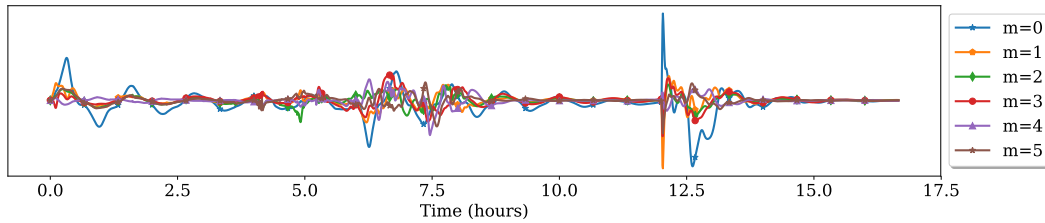
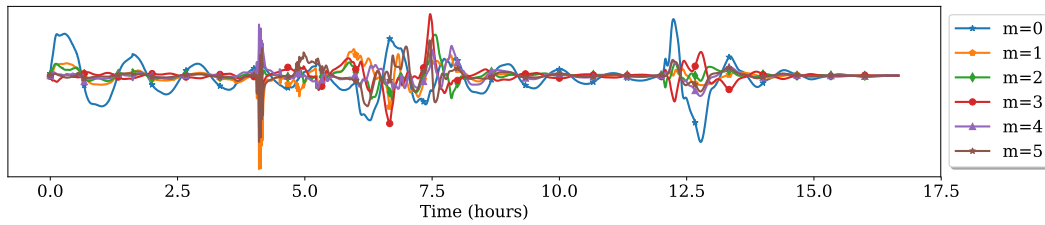


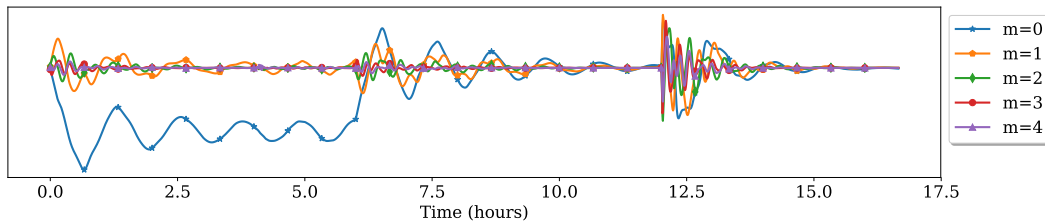
Figure 6: Temporal dynamics of the modal l^2 -norm of the time derivative of the projected solution snapshots for the Red River example



(a) First six modes of the projected x-velocity snapshots



(b) First six modes of the projected y-velocity snapshots



(c) First five modes of the projected depth snapshots

Figure 7: Dynamics captured by the modal time derivatives of the projected solution snapshots for the Red River example

To facilitate the modal residual driven iterations of the f-greedy and the psr-greedy algorithms, the contributions of the most dominant modes for each solution component towards

the overall flow behavior are studied. Figures 7a and 7b depict the evolution of the first six significant modes of the time derivative of the projected x- and y-velocity variables while Figure 7c shows the first five significant modes of the time derivative of the depth variable. The variations in the amplitude indicate that the first two significant modes capture most of the information about the temporal dynamics of the projected depth variable. On the other hand, at least the first three significant modes are needed to capture the temporal dynamics of the projected x-velocity. However, in order to include the flow characteristic represented by the local extremum, around $t = 4$ hours (see Figure 7b), it becomes necessary to consider at least the first four significant modes of the projected y-velocity variable.

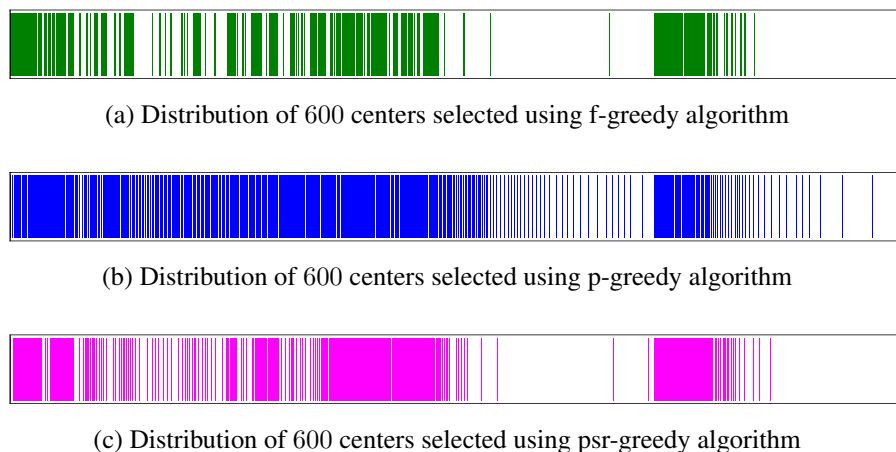


Figure 8: Comparative distribution of centers selected by the greedy algorithms for the Red River example

Figure 8 illustrates the temporal distribution of the first 600 centers selected by the three greedy algorithms. It is evident that the f-greedy (8a) and the psr-greedy (8c) centers are relatively more clustered around the locations of the local extrema in the l^2 -norm of the time derivative of the projected solution snapshots, shown in Figure 6. The p-greedy (8b) centers are more uniformly distributed all over the time domain. However, the online simulation period includes only the first two local extrema observed in Figure 6. Hence, the p-greedy NIROM solution is not able to approximate the high-fidelity solution as efficiently as the psr-greedy NIROM solution. The clustering effect is most pronounced for the f-greedy centers and the corresponding NIROM solution requires a lot more centers to achieve the desirable levels of accuracy.

Figure 9 illustrates this convergence behavior of the different greedy algorithms in terms of the $stRMSE$ norms (see eq. (40)) of the greedy NIROM solutions errors plotted with respect to the size of the RBF basis or the number of centers used by the RBF interpolant. The horizontal line represents the $stRMSE$ norm of a standard RBF NIROM solution in which 541 RBF centers were selected by uniformly skipping over every alternate snapshot from the projected high-fidelity solution set for the online time domain. As the p-greedy minimizes the overall approximation error using the power function, it performs better in the beginning. However, the psr-greedy algorithm produces a more optimal set of centers after the more dominant modal residuals have been optimized iteratively upto a chosen tolerance. The

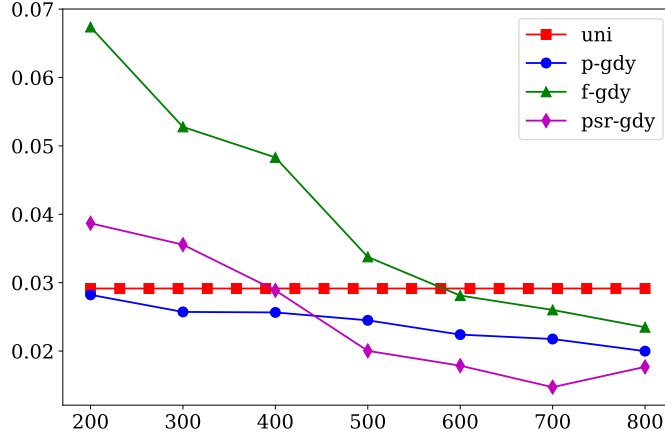


Figure 9: Convergence of the $stRMSE$ norm for the x -velocity variable computed using the different greedy NIROM solutions, with respect to the number of centers used by the RBF interpolant, for the Red River example

$stRMSE$ error norm for a RBF NIROM using all the available 1081 snapshots (following the approach of [49]) was also computed and the psr-greedy NIROM with 700 centers was still seen to be a better choice. In Table 3, the smallest $stRMSE$ error norms corresponding to all three components of the different greedy NIROM solutions are reported along with the respective sizes of the set of centers used in each case.

	<i>all</i> (1081)	<i>p-gdy</i> (800)	<i>f-gdy</i> (800)	<i>psr-gdy</i> (700)
\mathbf{u}_x	0.0155	0.0200	0.0235	0.0147
\mathbf{u}_y	0.0182	0.0240	0.0273	0.0176
\mathbf{h}	0.0080	0.0148	0.0116	0.0100

Table 3: Lowest $stRMSE$ error norms using each of the greedy NIROM solutions for the Red River example

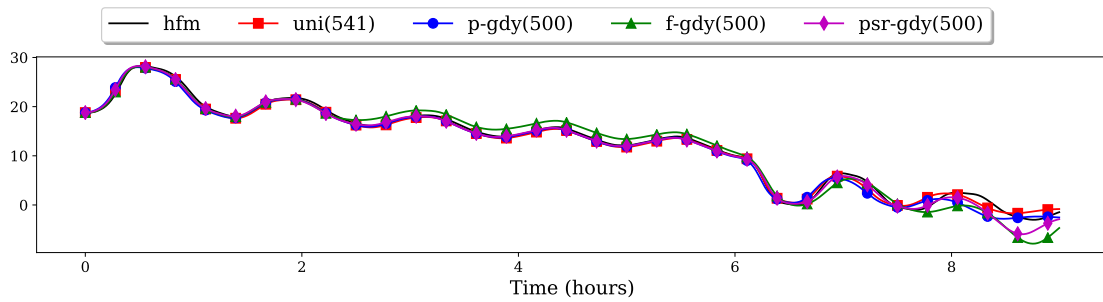
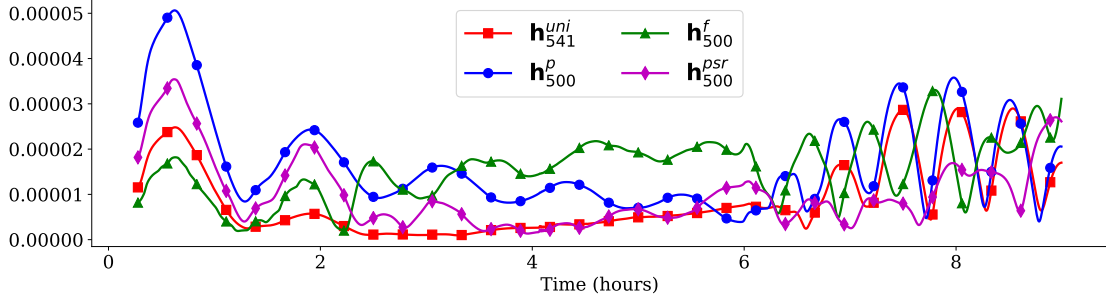
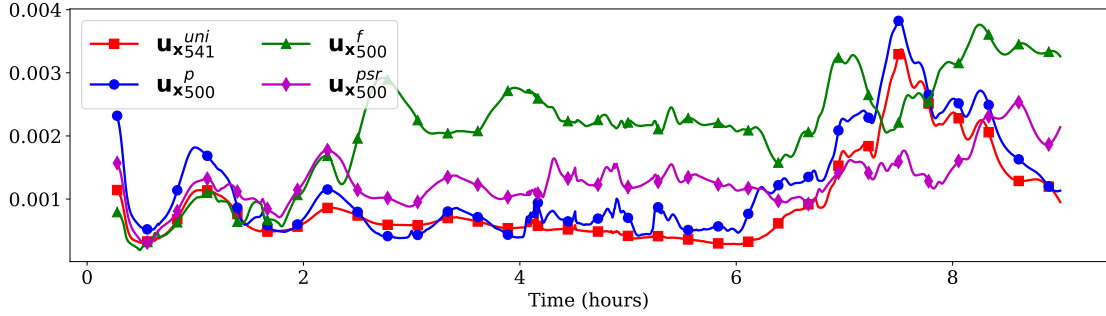


Figure 10: Comparison of the dominant mode of reduced x -velocity solutions for the Red River example

In order to compare the effectiveness of the different NIROM strategies in capturing the temporal dynamics of the high-fidelity solution, we consider greedy NIROM solutions that



(a) Comparison of the $wRMSE$ for the depth solutions



(b) Comparison of the $wRMSE$ for the x-velocity solutions

Figure 11: Temporal evolution of the spatial approximation errors of the NIROM solutions for the Red River example

use the first 500 selected centers and the standard RBF NIROM solution computed using alternatively-skipped 541 centers. Figure 10 compares the dominant mode of the reduced order NIROM solutions for the x-velocity to that obtained by projecting the high-fidelity solution on to the POD basis space (labelled as “hfm”). Figure 11 shows the temporal evolution of the weighted root mean square errors (see eq. 39) for the full order solution of the depth variable (Figure 11a) and the x-velocity variable (Figure 11b).

Figure 10 confirms that even using comparable number of centers all the greedy RBF NIROMs are almost equally effective in approximating the dominant features of the high-fidelity solution in the reduced basis (POD) space. Figures 11a and 11b provide a more detailed look into how the spatially-averaged RMS errors in the high-dimensional space evolve over time. The time derivatives of the first few dominant modes, as shown in Figure 7, depict a slowly varying, damped, periodic behavior during the initial stage of the flow, followed by a sudden, high-frequency, irregular flow phase starting at about $t = 6$ hours. The NIROM solutions generated by the uniformly spaced RBF centers and the power function driven RBF centers are able to approximate the initial damped, periodic flow phase with marginally higher accuracy. In the region with high-frequency variations, the uniformly distributed p-greedy centers are unable to provide sufficient resolution to effectively capture the flow dynamics. However, the residual driven RBF centers selected by the psr-greedy NIROM are able to capture the high-frequency, irregular variations in the solution more accurately and thus the psr-greedy NIROM offers a more stable and robust performance throughout the online time

domain. The f-greedy centers are clearly inadequate due to clustering and need to be further enriched in the under-represented locations by adopting a lower tolerance level, τ_f in order to achieve comparable levels of accuracy.

5.2.2. San Diego Bay Example

The final numerical example involves the simulation of tide-driven coastal flow in the San Diego Bay in California, USA (see Figure 12).

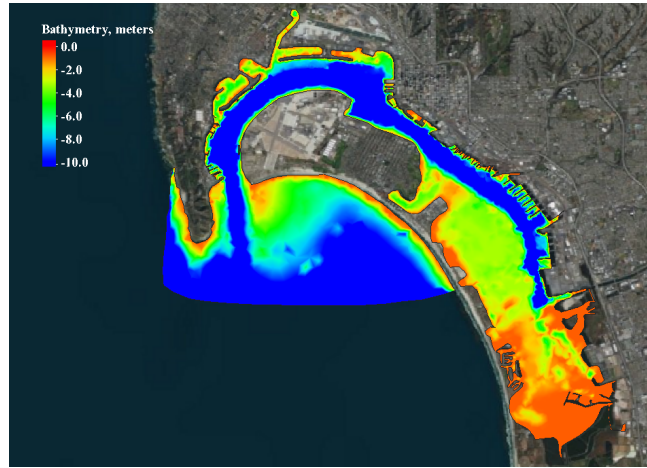


Figure 12: San Diego Bay

A uniform structured triangular mesh consisting of $N = 6311$ nodes and 10999 elements was used. Tidal flow data was obtained from NOAA/NOS Co-Ops website at an interval of 6 minutes. This was applied as a time series of tailwater elevation boundary data along the east-west boundary of the computational mesh at the entrance to the inner harbor, as shown in Figure 12. No flow boundary conditions were applied along the walls of the harbor and an initial water surface elevation for the entire domain was provided. The fluid viscosity $\nu = 10^{-5}$, Manning's friction coefficient $n_{nm} = 0.022$, and the Coriolis latitude is 32.7.

In the offline phase, the high-fidelity model was run until $T = 60$ hours with a time step of $\Delta t = 25$ seconds. Neglecting the first 100 time steps to avoid the influence of the initial startup on the flow behavior, 8540 offline solution snapshots were collected starting from an initial starting time of $t_0 = 2500$ seconds. The POD basis modes are computed using a subset of uniformly spaced 2136 snapshots that were selected by skipping over every 4 consecutive snapshots. Using a POD truncation tolerance of $\tau = 5 \times 10^{-3}$, only the first 29, 115 and 110 POD modes were selected for the reduced basis representation of the primitive variables \mathbf{h} , \mathbf{u}_x , and \mathbf{u}_y respectively. The online simulations were carried out from $t = 2500$ seconds to $t = 50$ hours with a time step of $\Delta t = 75$ seconds.

The subset of 2136 high-fidelity snapshots were projected onto the POD space to generate the set X containing all the available centers for the RBF interpolant. The p-greedy centers were selected using a tolerance of $\tau_p = 0.23$. A list of 18 dominant modes of the solution components \mathbf{u}_x , \mathbf{u}_y , \mathbf{h} were compiled by selecting the least number of modes for

each component that contain 91% of the total energy content for that component, *i.e.* using $\tau_{greedy} = 0.91$ in eq. (37). The residual computations for the f-greedy and the psr-greedy algorithms were carried out sequentially over this set of modes, $L = \{29, 144, 0, 30, 145, 1, 31, 146, 43, 147, 32, 154, 33, 156, 42, 150, 151, 165\}$. Here the modes of the projected depth snapshots lie between 0 to 28 out of which 2 modes are selected, x-velocity run from 29 to 143 from which 7 modes are selected, and y-velocity lie between 144 to 253 out of which 9 modes are selected.

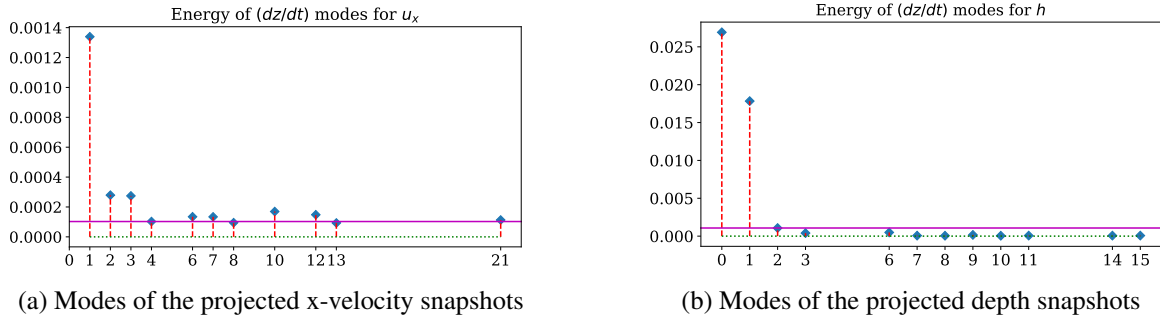


Figure 13: Comparison of the energy distribution in the most significant modes of the time derivative dz/dt for the projected x-velocity (left) and depth (right) snapshots of the San Diego Bay example

In Figure 13, 12 of the most “energetic” modes are plotted for each solution component, where the y-axis represents the energy content and the x-axis represents the respective modes. The 91% energy truncation is depicted by the horizontal line in each of the plots in Figure 13 such that the modal bars that fall above the line are selected for each component. In contrast to the visual identification method adopted in the Red River example, computing the energy content of the modes for each solution component using eq. (36) provides a numerical way to assess the relative significance of the individual modes. Depending on the desired level of accuracy and computational savings, it was observed that a list of modes capturing between 85% to about 95% of the total modal energy yielded an effective set of centers for the f-greedy and psr-greedy RBF NIROMS. The f-greedy and psr-greedy tolerances for terminating the modal iterations were taken to be $\tau_f = 0.41$ and $\tau_{psr} = 0.42$, respectively.

The modal l^2 -norms of the time derivatives of the projected snapshots for each solution component, as shown in Figure 14, highlight the periodic nature of the tide-driven flow. The higher frequency of the variations in the l^2 norms of the velocity components explain why a larger number of POD modes are required for the reduced basis representation of the velocity components as compared to the depth snapshots, and also why lesser number of depth modes are required in the f-greedy and psr-greedy modal residual computations.

Figure 15 depicts the distribution of the first 800 centers selected by the three greedy strategies. As expected, the f-greedy centers exhibit a clustering effect around the locations of the local extrema of the interpolated function, the p-greedy centers are much more uniformly distributed, and the psr-greedy approach moderates both these effects producing a less-scattered and less-clustered set of centers, as seen in Figure 15c. However, the periodic nature of the flow with relatively lower level of small-scale variations, offers a distinct

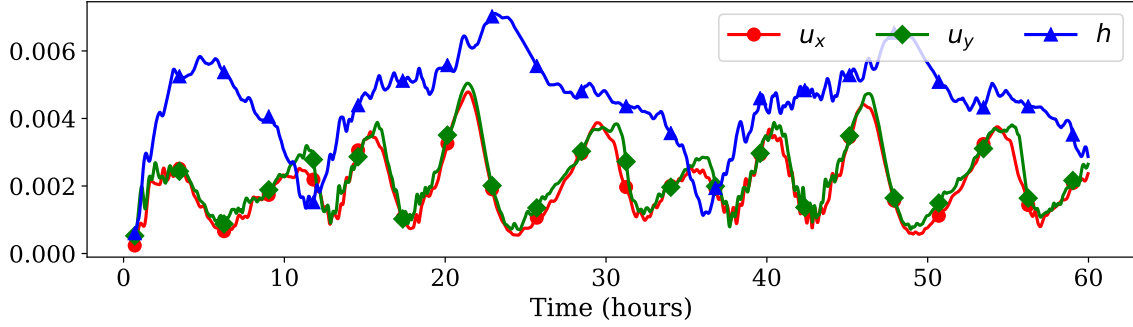


Figure 14: Temporal dynamics of the modal l^2 -norm of the time derivative of the projected solution snapshots for the San Diego Bay example



(a) Distribution of 800 centers selected using f-greedy algorithm



(b) Distribution of 800 centers selected using p-greedy algorithm



(c) Distribution of 800 centers selected using psr-greedy algorithm

Figure 15: Comparative distribution of centers selected by the greedy algorithms for the San Diego Bay example

advantage to the p-greedy selection procedure as shown below.

Figure 16 illustrates the convergence behavior of the different greedy algorithms in terms of the $stRMSE$ norms (see eq. (40)) of the greedy NIROM solutions errors. The x-axis shows the number of centers used by the RBF interpolant. The horizontal line represents the $stRMSE$ norm of a standard RBF NIROM solution in which 888 RBF centers were selected by uniformly skipping over every alternate snapshot from the projected high-fidelity solution set. The initial superior convergence rate of the p-greedy algorithm can be attributed to the relatively smoothly-varying periodic nature of the flow that is captured more efficiently by the uniformly distributed set of p-greedy centers. After the initial stage, the accuracy of the p-greedy NIROM doesn't improve any further with the selection of additional centers. In the psr-greedy algorithm, the convergence is more robust such that the $stRMSE$ steadily reduces with further enrichment of centers. Moreover, after the residual computations using the dominant modes capturing the key temporal dynamics for each component have been carried out, the psr-greedy selection is able to capture the small-scale features in the flow and hence the psr-greedy NIROM eventually offers superior accuracy than the other approaches. In Table 4, the smallest $stRMSE$ error norms corresponding to the x-velocity component of

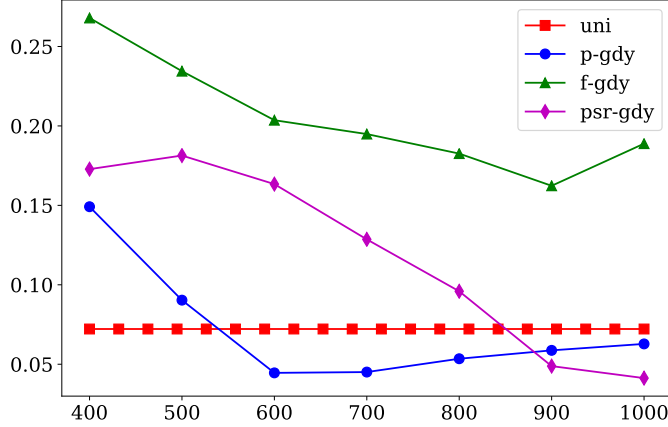


Figure 16: Convergence of the $stRMSE$ norm for the x -velocity variable computed using the different greedy NIROM solutions, with respect to the number of centers used by the RBF interpolant, for the San Diego Bay example

the different greedy NIROM solutions are reported along with the respective sizes of the set of centers used in each case. Additionally, $stRMSE$ norms are also reported for a standard RBF NIROM using all of the available 1776 centers and the previously described standard NIROM that uses 888 centers by skipping over alternate snapshots.

	<i>all</i> (1776)	<i>skipped</i> (888)	<i>p-gdy</i> (600)	<i>f-gdy</i> (900)	<i>psr-gdy</i> (1000)
\mathbf{u}_x	0.0309	0.0722	0.0446	0.1623	0.0413

Table 4: Lowest $stRMSE$ error norms using each of the greedy NIROM solutions for the San Diego Bay example

Figure 17 shows x -velocity solution obtained by psr-greedy NIROM at an intermediate time of around $t = 31$ hours, $19minutes$ and the error with respect to the high-fidelity solution. The localised structure of the flow features and error profile highlight the fact that in most practical applications, accurate modeling of specific regions in the flow domain is a more desirable outcome over a globally averaged and optimized model. This is where the psr-greedy NIROM can be truly beneficial as the selection of the data points for the interpolant is based on the minimization of the function residuals, constrained by preserving a well-conditioned kernel matrix.

Figure 18 compares the approximation of the dominant mode of the reduced depth solution over time using the greedy NIROMs and the alternatively skipped standard NIROM. The label “hfm” refers to the high-fidelity solution (true solution) projected on to the POD space. This offers validation that all the different NIROM procedures, with the exception of f-greedy NIROM, approximate the dominant features of the interpolated function relatively well.

Figure 19 shows the temporal evolution of the $wRMSE$ norms of the x -velocity solution, computed in the high dimensional space. The $wRMSE$ curves highlight the overall growth

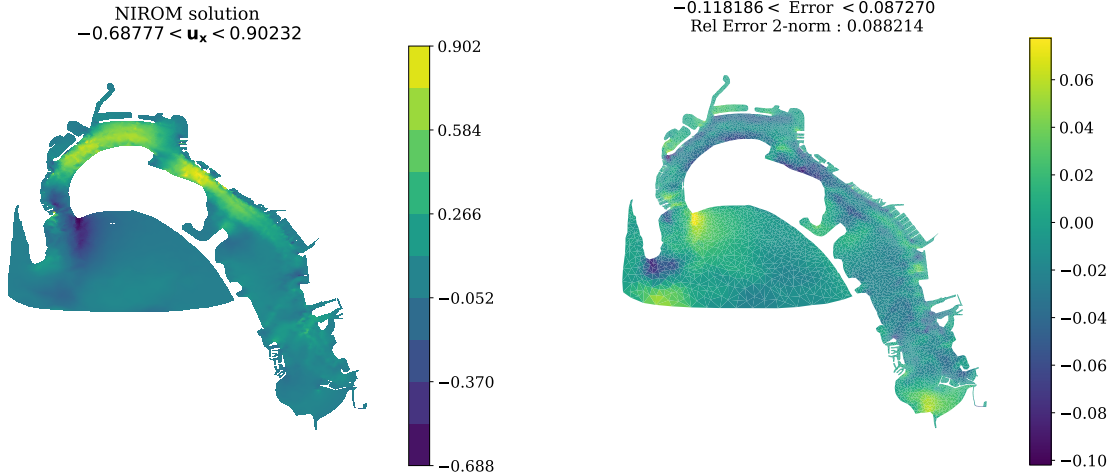


Figure 17: *psr-greedy* NIROM solutions for the x-velocity (left column) and the error (right column) with respect to the true solution at $t = 1.1275 \times 10^5$ seconds for the San Diego Bay example

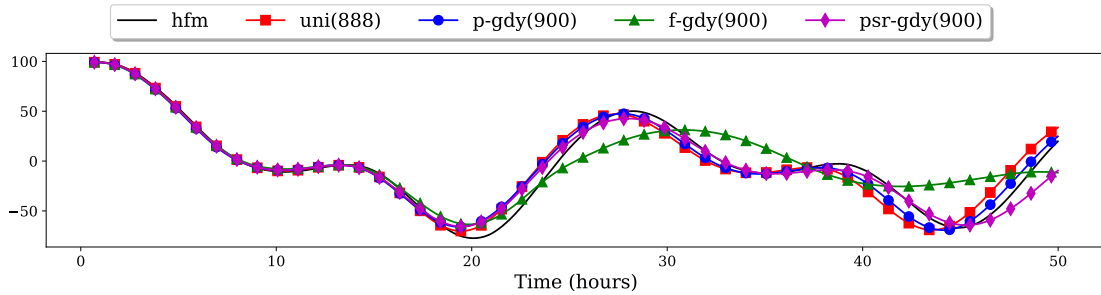


Figure 18: Comparison of the dominant mode of reduced depth solutions for the San Diego Bay example

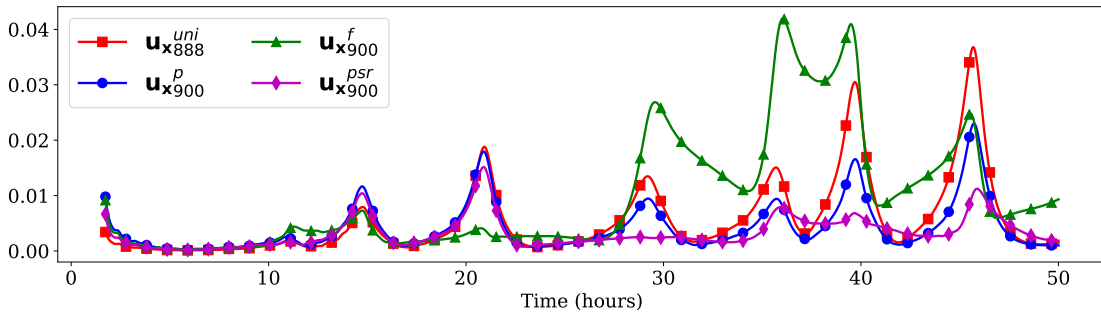


Figure 19: Temporal evolution of the $wRMSE$ of the x-velocity NIROM solutions for the San Diego Bay example

of approximation error over time, when RBF interpolation of the first order time derivatives of the reduced snapshots is adopted to model the temporal dynamics. However, the accuracy of the *psr-greedy* NIROM solution is relatively well preserved over time, as compared to the other NIROM solutions. These results emphasize another important feature of the *psr-greedy*

NIROM. Even for problems where the periodic nature of the temporal dynamics is a more natural fit for the kernel-driven center selection strategy of the p -greedy algorithm, the psr-greedy NIROM offers superior performance in terms of preserving accuracy over time as well as a steady reduction in error with the enrichment of data points.

6. Discussion

We briefly review some of the salient features of the greedy POD-RBF NIROM procedures and discuss some of the possible areas for future studies.

The simulations involving the greedy POD-RBF NIROMs, as reported in Section 5.2, were repeated with smaller tolerance levels for the POD truncation error. For instance, the San Diego Bay example was recomputed using a POD truncation error tolerance of $\tau = 10^{-6}$ such that 586, 820 and 808 POD modes were selected for the solution components \mathbf{h} , \mathbf{u}_x and \mathbf{u}_y respectively. While a marginal improvement in accuracy was observed, the relative trends in the performance of the greedy NIROMs were found to be similar to the results reported here. This provides a strong indication that the efficiency of the greedy RBF NIROM procedure for modeling the temporal dynamics is practically independent of the quality of the reduced basis representation of the high-fidelity snapshots. This property can help guide the design of optimal ROM parameters that can help strike a balance between computational reduction and desired accuracy of the ROM.

The proposed *psr-greedy* algorithm measures the dual effects of the RBF kernel as well as the function variability by defining the greedy metric to be a pointwise product of the power function and the modal residual errors. The power function acts as a variable scaling factor, enforcing the selected centers to be more widely distributed than the *f-greedy* algorithm and thus reducing the clustering effect, while a suitably chosen tolerance τ_{psr} ensures that regions of nonlinearity are more adequately resolved than the *p-greedy* algorithm. As a result, this algorithm performed consistently well and with superior efficiency in all of the different hydrodynamic regimes considered.

It was generally observed that any spatial measure of approximation error of the RBF NIROM solution grows with time. This is expected as the RBF interpolant is designed to approximate the discrete temporal derivative of the projected solution components. In this work, a first order accurate time discretization was adopted to compute the time derivative of the projected snapshots as well as to advance the reduced solutions in time (see eqs. (31) and (33)) which can cause the online evaluation error to accumulate sharply over time. This effect was subdued in the Red River example due to the overall growing intensity of the underlying flow, however, this effect was prominent in most of the greedy NIROM solutions for the periodic tidal flow simulations in the San Diego Bay example. One strategy to potentially arrest this growth would be to introduce a higher order time discretization scheme for the online model. On the other hand, one of the striking features of the psr-greedy NIROM was the ability to control this error growth and maintain a consistent level of accuracy throughout the online simulation period. This can be attributed to the fact that the first order time discretization error would also manifest in the time derivative function that was being interpolated, and since the psr-greedy NIROM is driven by the function residuals, it is able to counter this

growth by adequately increasing the resolution of selected centers in these regions of high residual error.

In both the numerical examples, the p-greedy NIROM exhibited a sharp initial convergence rate using very few centers. As the p-greedy strategy creates a quasi-uniform distribution of centers based on minimizing the error introduced by the kernel properties, it can rapidly identify the dominant features of the multidimensional interpolated function. On the other hand, the f-greedy and psr-greedy strategies need to iterate over the dominant modes in each solution component to effectively capture the salient features of the overall flow. While this can lead to slower convergence than p-greedy in the beginning, eventually this helps in achieving a steady rate of reduction in approximation error with gradual enrichment of the set of centers. However, the faster initial convergence of the p-greedy can be advantageous in constructing a ROM setup in applications where a very coarse approximation of the high-fidelity model is sufficient.

In all the greedy NIROM experiments, the shape factor of the RBF kernels is estimated conservatively as the fill distance of the set of all available centers, and is kept fixed at this value for all later computations using the different greedily selected center distributions. This conservative estimate was primarily adopted as the optimization of the shape factor was not the objective of this work. Additionally, the Matérn kernel is very well conditioned even when using flatter shape functions. Hence, there was no noticeable loss in the stability of the kernel computations while allowing for optimal performance in terms of accuracy of the RBF NIROMs. Keeping a fixed shape factor also facilitated easier comparison between the different greedy strategies and also between different levels of enrichment of data points for any given greedy strategy.

The efficiency of the RBF approximation may be further enhanced by increasing the flexibility of the radial kernel, so that significant changes in the rate of variability in the data as well as possible discontinuities can be represented more accurately. This may be achieved by considering Variably Scaled Kernels (VSK) [86] and Variably Scaled Discontinuous Kernels (VSDK) [87], which allow the shape factor c of the radial kernel to be variable across the domain. This method has the potential for some interesting applications in building predictive ROMs and is currently under investigation.

7. Conclusions

In this work, we have presented different greedy strategies for defining a POD-RBF non-intrusive reduced order model (NIROM) for a stabilized finite element approximation of the shallow water equations. The POD method is adopted to generate a suitable reduced basis space from the high-fidelity snapshots, and several greedy RBF interpolation strategies are developed to accurately model the temporal dynamics. We have compared the accuracy and the performance of the NIROM with a standard nonlinear POD (NPOD) ROM. We have also compared the performance of the greedy algorithms in determining a near-optimal m-term RBF approximation of the high-fidelity model in various challenging and realistic coastal and riverine flow problems. In our numerical experiments, we observed the following.

- (i) The relative ease of implementation of the POD-RBF NIROM makes it a desirable

choice for model reduction of time dependent problems in "fast-replay" scenarios, especially involving large scale legacy codes where access to the underlying source code maybe limited. Significant reduction in computational expense was achieved in comparison to the traditional nonlinear POD model.

- (ii) Three different greedy algorithms were studied as strategies of optimizing the distribution of centers for the RBF kernel. Using all the available centers [49] for interpolation often leads to redundant computational burden, which can be relieved by greedy center selection strategies, especially in the presence of nonlinear dynamics with varying temporal scales.
- (iii) The *f-greedy* algorithm is designed to directly minimize the functional approximation errors or residuals in order to select the RBF centers. This leads to a clustering problem due to oversampling of centers around regions of strong nonlinearity in the solution. Hence the f-greedy algorithm suffers from an undesirable loss in efficiency.
- (iv) The *p-greedy* algorithm is aimed at selecting centers by minimizing the power function, which converges towards a fairly uniform distribution with every greedy iteration. Hence, this algorithm may suffer from under-sampling in regions of strong nonlinearity. Thus, an initial strong convergence rate is followed by a loss in efficiency and no significant improvement in accuracy.
- (v) The proposed *psr-greedy* algorithm reduces the clustering effect while improving resolution in under-sampled areas to generate a well-balanced set of centers. This algorithm displayed robust convergence and superior efficiency in problems involving both coastal and riverine scales, making it the best candidate for obtaining an optimal distribution of centers for the RBF kernel.

8. Acknowledgments

This research was supported in part by an appointment of the first author to the Postgraduate Research Participation Program at the U.S. Army Engineer Research and Development Center, Coastal and Hydraulics Laboratory (ERDC-CHL) administered by the Oak Ridge Institute for Science and Education through an interagency agreement between the U.S. Department of Energy and ERDC. The research contributions by the third and the fifth authors have been accomplished within Rete Italiana di Approssimazione (RITA), partially funded by GNCS-IN δ AM and through the European Union's Horizon2020 research and innovation programme ERA-PLANET, grant agreement no. 689443, via the GEOEssential project. The authors would also like to thank Corey Trahan for his valuable help in using the Adaptive Hydraulics suite (AdH) [59, 88, 89] for the high-fidelity numerical simulation of the 2D shallow water flow examples. Permission was granted by the Chief of Engineers to publish this information.

References

- [1] G. Savant, R. Berger, T. McAlpin, J. Tate, Efficient implicit finite-element hydrodynamic model for dam and levee breach, *J. Hydraulic Eng.* 137 (9) (2011) 1005–1018.
- [2] J. J. Westerink, R. A. Luettich, J. C. Feyen, J. H. Atkinson, C. N. Dawson, H. J. Roberts, M. D. Powell, J. P. Dunion, E. J. Kubatko, H. Pourtaheri, A basin- to channel-scale unstructured grid hurricane storm surge model applied to southern Louisiana, *Monthly Weather Review* 136 (2008) 833–864.
- [3] C. Vreugdenhil, *Numerical Methods for Shallow-Water Flow*, Kluwer Academic Publishers, 1992.
- [4] A. Quarteroni, A. Manzoni, F. Negri, *Reduced Basis Methods for Partial Differential Equations*, Springer, Cham, 2016. doi:10.1007/978-3-319-15431-2.
- [5] S. Razavi, B. Tolson, D. Burn, Review of surrogate modeling in water resources, *Water Resources Res.* 48 (7) (2012) n/a–n/a, w07401. doi:10.1029/2011WR011527.
- [6] P. Benner, S. Gugercin, K. Willcox, A survey of projection-based model reduction methods for parametric dynamical systems, *SIAM Rev.* 57 (4) (2015) 483–531.
- [7] J. Eftang, D. Knezevic, A. Patera, An hp certified reduced basis method for parametrized parabolic partial differential equations, *Math. Comput. Modelling Dyn. Sys.* 17 (4) (2011) 395–422. doi:10.1080/13873954.2011.547670.
- [8] B. Haasdonk, M. Oehlberger, Reduced basis method for finite volume approximations of parametrized linear evolution equations, *ESAIM Math. Model. Numer. Anal.* 42 (2008) 277–302. doi:10.1051/m2an:2008001.
- [9] G. Berkooz, P. Holmes, J. Lumley, The proper orthogonal decomposition in the analysis of turbulent flows, *Annu. Rev. Fluid Mech.* 25 (1) (1993) 539–575. doi:10.1146/annurev.fl.25.010193.002543.
- [10] Y. Liang, H. Lee, S. Lim, W. Lin, K. Lee, C. Wu, Proper Orthogonal Decomposition and Its Applications-Part I: Theory, *J. Sound Vib.* 252 (3) (2002) 527–544. doi:10.1006/jsvi.2001.4041.
- [11] L. Sirovich, Turbulence and the dynamics of coherent structures. Part I:Coherent structures, *Quart. Appl. Math.* 45 (1987) 561–571.
- [12] I. Jolliffe, *Principal Component Analysis*, Springer New York, USA, 1986.
- [13] P. Deheuvels, G. Martynov, A Karhunen-Loeve decomposition of a Gaussian process generated by independent pairs of exponential random variables, *J. Func. Anal.* 255 (9) (2008) 2363–2394. doi:10.1016/j.jfa.2008.07.021. URL <http://dx.doi.org/10.1016/j.jfa.2008.07.021>
- [14] P. Vermeulen, A. Heemink, Model-reduced variational data assimilation, *Monthly Weather Review* 134 (2006) 2888–2899.

- [15] F. Fang, T. Zhang, D. Pavlidis, C. Pain, A. Buchanan, I. Navon, Reduced order modelling of an unstructured mesh air pollution model and application in 2D/3D urban street canyons, *Atmos. Env.* 96 (2014) 96–106.
- [16] O. San, J. Borggaard, Principal interval decomposition framework for POD reduced-order modeling of convective Boussinesq flow, *Int. J. Numer. Methods Fluids* 78 (1) (2015) 37–62.
- [17] D. Bistriani, I. Navon, An improved algorithm for the shallow water equations model reduction: Dynamic Mode Decomposition vs POD, *Int. J. Numer. Methods Fluids* (2015).
- [18] R. Stefanescu, A. Sandu, I. Navon, Comparison of POD reduced order strategies for the nonlinear 2D shallow water equations, *Int. J. Numer. Methods Fluids* 76 (8) (2014) 497–521.
- [19] M. Ghasemi, Y. Yang, E. Gildin, Y. Efendiev, V. Calo, Fast Multiscale Reservoir Simulations using POD-DEIM Model Reduction, in: *SPE Res. Sim. Symp.*, no. December, 2015. doi:10.2118/173271-MS.
- [20] A. Lozovskiy, M. Farthing, C. Kees, E. Gildin, POD-based model reduction for stabilized finite element approximations of shallow water flows, *J. Comput. Appl. Math.* 302 (2016) 50–70.
- [21] A. Lozovskiy, M. Farthing, C. Kees, Evaluation of Galerkin and Petrov-Galerkin model reduction for finite element approximations of the shallow water equations, *Comput. Methods Appl. Mech. Eng.* 318 (2017) 537–571. doi:10.1016/j.cma.2017.01.027.
- [22] B. Koopman, Hamiltonian Systems and Transformation in Hilbert Space., *Proc. Natl. Acad. Sci. U. S. A.* 17 (5) (1931) 315–8.
- [23] C. Rowley, I. Mezi, S. Bagheri, P. Schlatter, D. Henningson, Spectral analysis of nonlinear flows, *J. Fluid Mech.* 641 (Rowley 2005) (2009) 115–127. doi:10.1017/S0022112009992059.
- [24] P. Schmid, Dynamic mode decomposition of numerical and experimental data, *J. Fluid Mech.* 656 (July 2010) (2010) 5–28. doi:10.1109/PIERS-FALL.2017.8293532.
- [25] S. Bagheri, Koopman-mode decomposition of the cylinder wake, *J. Fluid Mech.* 726 (2013) 596–623. doi:10.1017/jfm.2013.249.
- [26] A. Alekseev, D. Bistriani, A. Bondarev, I. Navon, On linear and nonlinear aspects of dynamic mode decomposition, *Int. J. Numer. Methods Fluids* 82 (6) (2016) 348–371. doi:10.1002/flid.4221.
- [27] D. Bistriani, I. Navon, The method of dynamic mode decomposition in shallow water and a swirling flow problem, *Int. J. Numer. Methods Fluids* (2017) DOI:10.1002/flid.4257.
- [28] N. Erichson, C. Donovan, Randomized low-rank Dynamic Mode Decomposition for motion detection, *Comput. Vis. Image Underst.* 146 (2016) 40–50. doi:10.1016/j.cviu.2016.02.005.
- [29] D. Bistriani, I. Navon, Randomized dynamic mode decomposition for nonintrusive reduced order modelling, *Int. J. Numer. Methods Eng.* 112 (2017) 3–25. doi:10.1002/nme.5499.

- [30] D. Amsallem, M. Zahr, Y. Choi, C. Farhat, Design optimization using hyper-reduced-order models, *Struct. Multi. Opt.* 51 (4) (2015) 919–940. doi:10.1007/s00158-014-1183-y.
- [31] M. Barrault, Y. Maday, N. Nguyen, A. Patera, An ‘empirical interpolation’ method: application to efficient reduced-basis discretization of partial differential equations, *Comptes Rendus Mathematique* 339 (9) (2004) 667–672.
- [32] S. Chaturantabut, D. Sorensen, Nonlinear model reduction via Discrete Empirical Interpolation, *SIAM J. Sci. Comput.* 32 (5) (2010) 2737–2764. doi:10.1137/090766498.
- [33] K. Willcox, Unsteady flow sensing and estimation via the gappy Proper Orthogonal Decomposition, *Comput. Fluids* 35 (2) (2006) 208–226.
- [34] N. Nguyen, J. Peraire, An efficient reduced-order modeling approach for non-linear parametrized partial differential equations, *Int. J. Numer. Methods Eng.* 76 (2008) 27–55. doi:10.1002/nme.2309.
- [35] D. Xiao, F. Fang, A. Buchan, C. Pain, I. Navon, J. Du, G. Hu, Non-linear model reduction for the Navier-Stokes equations using residual DEIM method, *J. Comput. Phys.* 263 (2014) 1–18. doi:10.1016/j.jcp.2014.01.011.
- [36] F. Ballarin, A. Manzoni, A. Quarteroni, G. Rozza, Supremizer stabilization of POD-Galerkin approximation of parametrized steady incompressible Navier-Stokes equations, *Int. J. Numer. Methods Eng.* 102 (2015) 1136–1161. doi:10.1002/nme.4772.
- [37] M. Barone, I. Kalashnikova, D. Segalman, H. Thornquist, Stable Galerkin reduced order models for linearized compressible flow, *J. Comput. Phys.* 228 (6) (2009) 1932–1946. doi:10.1016/j.jcp.2008.11.015.
- [38] D. Amsallem, C. Farhat, Stabilization of projection-based reduced order models, *Int. J. Numer. Methods Eng.* 91 (2012) 358–377. doi:10.1002/nme.4274.
- [39] D. Xiao, F. Fang, J. Du, C. Pain, I. Navon, A. Buchan, A. ElSheikh, G. Hu, Non-linear Petrov-Galerkin methods for reduced order modelling of the Navier-Stokes equations using a mixed finite element pair, *Comput. Methods Appl. Mech. Eng.* 255 (2013) 147–157. doi:10.1016/j.cma.2012.11.002.
- [40] F. Fang, C. Pain, I. Navon, A. ElSheikh, J. Du, D. Xiao, Non-linear Petrov-Galerkin methods for reduced order hyperbolic equations and discontinuous finite element methods, *J. Comput. Phys.* 234 (2013) 540–559. doi:10.1016/j.jcp.2012.10.011.
- [41] K. Carlberg, C. Bou-Mosleh, C. Farhat, Efficient non-linear model reduction via a least-squares Petrov-Galerkin projection and compressive tensor approximations, *Int. J. Numer. Methods Eng.* 86 (2011) 155–181. doi:10.1002/nme.3050.
- [42] J. Hesthaven, S. Ubbiali, Non-intrusive reduced order modeling of nonlinear problems using neural networks, *J. Comput. Phys.* 363 (2018) 55–78. doi:10.1016/j.jcp.2018.02.037.

- [43] M. Guo, J. Hesthaven, Reduced order modeling for nonlinear structural analysis using Gaussian process regression, *Comput. Methods Appl. Mech. Eng.* 341 (January 2018) (2018) 807–826. doi:10.1016/j.cma.2018.07.017.
- [44] M. Guo, J. Hesthaven, Data-driven reduced order modeling for time-dependent problems, *Comput. Methods Appl. Mech. Eng.* 345 (2019) 75–99. doi:10.1016/j.cma.2018.10.029.
- [45] F. Narcowich, J. Ward, Scattered-data interpolation on \mathbb{R}^n : Error estimates for radial basis and band-limited functions, *SIAM J. Math. Anal.* 36 (1) (2004) 284–300.
- [46] E. Larsson, B. Fornberg, A numerical study of some radial basis function based solution methods for elliptic PDEs, *Comput. Math. with Appl.* 46 (5-6) (2003) 891–902. doi:10.1016/S0898-1221(03)90151-9.
- [47] V. Shankar, G. Wright, A. Fogelson, R. Kirby, A radial basis function (rbf) finite difference method for the simulation of reaction-diffusion equations on stationary platelets within the augmented forcing method, *Int. J. Numer. Methods Fluids* 75 (1) (2014) 1–22. doi:10.1002/flid.3880.
- [48] M.J. Er, S. Wu, J. Lu, H.L. Toh, Face recognition with radial basis function (RBF) neural networks, *IEEE Trans. Neu. Net.* 13 (3) (2002) 697–710. doi:10.1109/tnn.2002.1000134.
- [49] D. Xiao, F. Fang, C. Pain, G. Hu, Non-intrusive reduced-order modelling of the Navier-Stokes equations based on RBF interpolation, *Int. J. Numer. Methods Fluids* 79 (2015) 580–595. doi:10.1002/flid.406.
- [50] C. Audouze, F. De Vuyst, P. Nair, Nonintrusive Reduced-Order Modeling of Parametrized Time-Dependent Partial Differential Equations, *Numer. Methods Partial Differ. Equasion* 29 (5) (2013) 1587–1628. doi:10.1002/num.21768.
- [51] D. Xiao, F. Fang, C. Pain, I. Navon, A parameterized non-intrusive reduced order model and error analysis for general time-dependent nonlinear partial differential equations and its applications, *Comput. Methods Appl. Mech. Eng.* 317 (2017) 868–889. doi:10.1016/j.cma.2016.12.033.
- [52] W. Chen, J. Hesthaven, B. Junqiang, Z. Yang, Y. Tihao, A Greedy Non-Intrusive Reduced Order Model for Fluid Dynamics, *AIAA J.* 56 (12) (2018) 1–39. doi:10.2514/1.J056161.
- [53] E. Iuliano, D. Quagliarella, Aerodynamic shape optimization via non-intrusive POD-based surrogate modelling, in: 2013 IEEE Congr. Evol. Comput. CEC 2013, IEEE, 2013, pp. 1467–1474. doi:10.1109/CEC.2013.6557736.
- [54] C. Trahan, G. Savant, R. Berger, M. Farthing, T. McAlpin, L. Pettey, G. Choudhary, C. Dawson, Formulation and application of the adaptive hydraulics three-dimensional shallow water and transport models, *J. Comput. Phys.* 374 (2018) 47–90. doi:10.1016/j.jcp.2018.04.055.
- [55] S. Bova, G. Carey, A symmetric formulation and SUPG scheme for the shallow-water equations, *Adv. Water Resour.* 19 (3) (1996) 123–131. doi:10.1016/0309-1708(95)00040-2.

- [56] T. Hughes, M. Mallet, A new finite element formulation for computational fluid dynamics: III. The generalized streamline operator for multidimensional advective-diffusive systems, *Comput. Methods Appl. Mech. Eng.* 58 (3) (1986) 305–328.
- [57] S. De Marchi, R. Schaback, H. Wendland, Near-optimal data-independent point locations for radial basis function interpolation, *Adv. Comput. Math.* 23 (3) (2005) 317–330. doi:10.1007/s10444-004-1829-1.
- [58] R. Schaback, H. Wendland, Adaptive greedy techniques for approximate solution of large RBF systems, *Numer. Algorithms* 24 (3) (2000) 239–254. doi:10.1023/A:1019105612985.
- [59] G. Savant, R. Berger, T. McAlpin, J. Tate, Efficient Implicit Finite-Element Hydrodynamic Model for Dam and Levee Breach, *J. Hydraulic Eng.* 137 (9) (2011) 1005–1018. doi:10.1061/(asce)hy.1943-7900.0000372.
- [60] V. Aizinger, C. N. Dawson, A discontinuous Galerkin method for two-dimensional flow and transport in shallow water, *Adv. Water Res.* 25 (1) (2002) 67–84.
- [61] R. Berger, R. Stockstill, Finite element model for high-velocity channels, *J. Hydraulic Eng.* 121 (10) (1995).
- [62] T. Hughes, G. Feijóo, L. Mazzei, J.-B. Quincy, The variational multiscale method – a paradigm for computational mechanics, *Comput. Methods Appl. Mech. Eng.* 166 (1) (1998) 3–24.
- [63] A. Antoulas, D. Sorensen, Approximation of large-scale dynamical systems: An overview, *Int. J. Appl. Math. Comput. Sci.* 11 (5) (2001) 1093–1121.
- [64] T. Lassila, M. A., A. Quarteroni, G. Rozza, Model order reduction in fluid dynamics: challenges and perspectives, in: *Reduced Order Methods for Modeling and Computational Reduction*, Vol. 9 of MS&A Series, Springer Verlag, 2014, pp. 235–274.
- [65] K. Carlberg, C. Farhat, J. Cortial, D. Amsallem, The GNAT method for nonlinear model reduction: Effective implementation and application to computational fluid dynamics and turbulent flows, *J. Comput. Phys.* 242 (2013) 623–647. doi:10.1016/j.jcp.2013.02.028.
- [66] G. Dimitriu, R. Ștefănescu, I. Navon, Comparative numerical analysis using reduced-order modeling strategies for nonlinear large-scale systems, *J. Comput. Appl. Math.* 310 (2017) 32–43. doi:10.1016/j.cam.2016.07.002.
- [67] K. Carlberg, C. Farhat, D. Amsallem, The GNAT method for nonlinear model reduction: effective implementation to computational fluid dynamics and turbulent flows, *J. Comput. Phys.* 242 (2013) 623–647.
- [68] R. Carlson, T. Foley, The parameter R^2 in multiquadric interpolation, *Comput. Math. with Appl.* 21 (9) (1991) 29–42. doi:10.1016/0898-1221(91)90123-L.
- [69] G. Fasshauer, *Meshfree Approximation Methods with MATLAB*, Vol. 6 of *Interdisciplinary Mathematical Sciences*, World Scientific Publishing Company, 2007.

- [70] D. Wirtz, B. Haasdonk, A Vectorial Kernel Orthogonal Greedy Algorithm, *Dolomites Res. Notes Approx.* 6 (2013) 83–100. doi:10.14658/pupj-drna-2013-Special{_}Issue-10.
- [71] H. Wendland, *Scattered Data Approximation*, Cambridge University Press, 2005.
- [72] R. DeVore, Nonlinear approximation, *Acta Numer.* 7 (1998) 51–150. doi:10.1017/S0962492900002816.
- [73] M. Floater, A. Iske, Thinning algorithms for scattered data interpolation, *BIT Numer. Math.* 38 (4) (1998) 705–720. doi:10.1007/BF02510410.
- [74] E. Lim, Z. Zainuddin, An Improved Fast Training Algorithm for RBF Networks Using Symmetry-Based Fuzzy C-Means Clustering, *Matematika* 24 (2) (2008) 141–148.
- [75] H. Liu, J. He, The application of dynamic K-means clustering algorithm in the center selection of RBF neural networks, 3rd Int. Conf. Genet. Evol. Comput. WGECC 2009 (2009) 488–491 doi: 10.1109/WGECC.2009.112.
- [76] J. Sing, D. Basu, M. Nasipuri, M. Kundu, Improved k-means algorithm in the design of RBF neural networks, in: *TENCON 2003. Conf. Converg. Technol. Asia-Pacific Reg.*, 2003, pp. 841–845. doi:10.1109/tencon.2003.1273297.
- [77] J. Tropp, A. Gilbert, M. Strauss, Algorithms for simultaneous sparse approximation. Part I: Greedy pursuit, *Signal Proc.* 86 (3) (2006) 572–588. doi:10.1016/j.sigpro.2005.05.030.
- [78] V. Temlyakov, Greedy approximation, *Acta Numer.* 17 (2008) 235–409. doi:10.1017/S0962492906380014.
- [79] G. Santin, B. Haasdonk, Convergence rate of the data-independent P -greedy algorithm in kernel-based approximation, *Dolomites Res. Notes Approx.* 10 (2) (2017) 68–78. doi:10.14658/pupj-drna-2017-Special{_}Issue-9.
- [80] M. Shahrokhbadi, A. Neisy, E. Perracchione, M. Polato, Learning with subsampled kernel-based methods: Environmental and financial applications, *Dolomites Res. Notes Approx.* 12 (1) (2019) 17–27.
- [81] D. Leviatan, V. Temlyakov, Simultaneous greedy approximation in Banach spaces, *J. Complex.* 21 (3) (2005) 275–293. doi:10.1016/j.jco.2004.09.004.
- [82] R. Schaback, J. Werner, Linearly constrained reconstruction of functions by kernels with applications to machine learning, *Adv. Comput. Math.* 25 (1-3) (2006) 237–258. doi:10.1007/s10444-004-7616-1.
- [83] M. Pazouki, R. Schaback, Bases for kernel-based spaces, *J. Comput. Appl. Math.* 236 (4) (2011) 575–588. doi:10.1016/j.cam.2011.05.021.
- [84] S. Walton, O. Hassan, K. Morgan, Reduced order modelling for unsteady fluid flow using proper orthogonal decomposition and radial basis functions, *Appl. Math. Model.* 37 (20-21) (2013) 8930–8945. doi:10.1016/j.apm.2013.04.025.

- [85] T. McAlpin, J. Sharp, S. Scott, G. Savant, Habitat restoration and flood control protection in the Kissimmee river, *Wetlands* 33 (3) (2013) 551–560. doi:10.1007/s13157-013-0412-2.
- [86] M. Bozzini, L. Lenarduzzi, M. Rossini, R. Schaback, Interpolation with variably scaled kernels, *IMA J. Numer. Anal.* 35 (1) (2015) 199–219. doi:10.1093/imanum/drt071.
- [87] S. De Marchi, A. Martínez, E. Perracchione, Fast and stable rational RBF-based partition of unity interpolation, *J. Comput. Appl. Math.* 349 (2019) 331–343. doi:10.1016/j.cam.2018.07.020.
- [88] G. Savant, R. Berger, Adaptive Time Stepping-Operator Splitting Strategy to Couple Implicit Numerical Hydrodynamic and Water Quality Codes, *J. Environ. Eng.* 138 (9) (2012) 979–984. doi:10.1061/(asce)ee.1943-7870.0000547.
- [89] J. Tate, R. Berger, R. Stockstill, Refinement indicator for mesh adaption in shallow-water modeling, *J. Hydraulic Eng.* 132 (8) (2006) 854–857. doi:10.1061/(ASCE)0733-9429(2006)132:8(854).